

Buoyancy-driven exchange flows in inclined ducts

Adrien Lefauve¹ and P. F. Linden¹

¹Department of Applied Mathematics and Theoretical Physics, University of Cambridge
Centre for Mathematical Sciences, Wilberforce Road, Cambridge, CB3 0WA, UK.

(Received xx; revised xx; accepted xx)

Buoyancy-driven exchange flows arise in the natural and built environment wherever bodies of fluids at different densities are connected by a narrow constriction. In this paper we study these flows in the laboratory using the canonical stratified inclined duct experiment, which sustains an exchange flow in an inclined duct of rectangular cross-section over long time periods (Meyer & Linden, *J. Fluid Mech.*, vol. 753, 2014). We study the behaviour of these sustained stratified shear flows by focusing on three dependent variables of particular interest: the qualitative flow regime (laminar, wavy, intermittently turbulent, or fully turbulent), the mass flux (net transport of buoyancy between reservoirs), and the interfacial thickness (thickness of the layer of intermediate density between the two counter-flowing layers). Dimensional analysis reveals five non-dimensional independent input parameters: the duct aspect ratios in the longitudinal direction A and spanwise direction B , the tilt angle θ , the Reynolds number Re (based on the initial buoyancy difference driving the flow), and the Prandtl number Pr (we consider both salt and temperature stratifications). After reviewing the literature and open questions on the scaling of regimes, mass flux, and interfacial thickness with A, B, θ, Re, Pr , we present the first extensive, unified set of experimental data where we varied systematically all five input parameters and measured all three output variables with the same methodology. Our results in the (θ, Re) plane for five sets of (A, B, Pr) reveal a variety of scaling laws, and a non-trivial dependence of all three variables on all five parameters, in addition to a sixth elusive parameter. We further develop three classes of candidate models to explain the observed scaling laws: (i) the recent volume-averaged energetics of Lefauve, Partridge & Linden, *J. Fluid Mech.*, 2019; (ii) two-layer frictional hydraulics; (iii) turbulent mixing models. While these models provide significant qualitative and quantitative descriptions of the experimental results, they also highlight the need for further progress on shear-driven turbulent flows and their interfacial waves, layering, intermittency, and mixing properties.

Key words:

1. Introduction

Buoyancy-driven exchange flows naturally arise where relatively large bodies of fluid have different densities on either side of a relatively narrow constriction. In a gravitational field, this difference in buoyancy, usually in the horizontal direction, results in a horizontal hydrostatic pressure gradient along the constriction, of opposite sign above and below a ‘neutral level’, a height at which the pressures on either side of the constriction are equal. This pressure gradient drives a counter-flow through the constriction, in which fluid from the negatively-buoyant reservoir flows below the neutral level towards the positively-buoyant reservoir, and conversely, with equal magnitude. Such buoyancy-driven exchange

42 flows result in little to no net volume transport, but crucially, in a *net buoyancy transport*
 43 between the reservoirs which tends to homogenise buoyancy differences in the system (i.e.
 44 towards equilibrium). In addition, *irreversible mixing* often occurs across the interface
 45 between the two counter-flowing layers of fluid, creating an intermediate layer of partially
 46 mixed fluid, and partially reducing the buoyancy transport. The net transport and
 47 mixing of the active scalar field (e.g. heat, salt, or other solutes) and of other potential
 48 passive scalar fields having different concentrations in either reservoirs (e.g. pollutants
 49 or nutrients) have a wide range of consequences of interest. For this reason, the study of
 50 buoyancy-driven exchange flows has a rich history. (The primary role of buoyancy being
 51 implicit throughout the paper, we will simply refer to these flows as ‘exchange flows’.)

52 Aristotle offered the first recorded explanation of the movement of salty water within
 53 the Mediterranean Sea (Deacon 1971, pp. 8-9). Ever since, exchange flows through the
 54 straits of Gibraltar and the Bosphorus have driven much speculation and research, due
 55 to their crucial roles in the water and salt balances of the Mediterranean Sea, countering
 56 its evaporation by net volume transport and allowing its very existence (as first demon-
 57 strated experimentally by Marsigli in the 1680s (Deacon 1971, Chap. 7)). More recently,
 58 it has been recognised that nutrient transport from the Atlantic partially supported
 59 primary production in Mediterranean ecosystems (Estrada 1996). The quantification,
 60 modelling, and discussion of the past and current impact of exchange flows in straits,
 61 estuaries, or between lakes continues to generate a vast literature.

62 Exchange flows of *gases* also have a great variety of perhaps even more tangible and
 63 ancient applications to society in the ‘natural ventilation’ of buildings (Linden 1999).
 64 It would be surprising indeed if some ice-age prehistoric *Homo Sapiens* did not ponder
 65 the inflow of cold outside air and the outflow of heat or fire combustion products when
 66 choosing a cave suitable for living. More recently, engineering problems of air flow through
 67 open doorways or ventilation ducts, or the escape of gases from ruptured industrial pipes,
 68 have stimulated further research.

69 More fundamentally, exchange flows are stably-stratified shear flows, a canonical class
 70 of flows widely used in the mathematical study of stratified turbulence, dating back at
 71 least to (Reynolds 1883, § 12) and Taylor (1931). Multi-layered stratified shear flows
 72 have complex hydrodynamic stability and turbulent mixing properties (Caulfield 1994;
 73 Peltier & Caulfield 2003). The straightforward and steady forcing of exchange flows make
 74 them ideal laboratory stratified shear flows because of the ability to sustain, over long
 75 time periods, high levels of turbulent intensity and mixing representative of large-scale
 76 natural flows.

77 The aim of this paper is to carry out a thorough review and exploratory study of
 78 buoyancy-driven exchange flows in inclined ducts. To do this, we will focus on the
 79 behaviour of three key variables:

- 80 (i) the qualitative flow regime (e.g. laminar, wavy, intermittently or fully turbulent);
- 81 (ii) the mean buoyancy transport;
- 82 (iii) the mean thickness of any potential interfacial mixing layer.

83 The above three variables are particularly relevant in applications to predict exchange
 84 rates of active or passive scalars (e.g. salt, heat, pollutants, nutrients) between two
 85 different fluid bodies (e.g. rooms in a building, seas or lakes on either sides of a strait).

86 However, our primary motivation in this paper is to contribute to a larger research
 87 effort into the fundamental properties of turbulence in sustained stratified shear flows
 88 of geophysical relevance. The above three variables have thus been chosen for their
 89 particular ability to be readily captured by simple laboratory techniques while encapsu-
 90 lating several key flow features that are currently the subject of active research, such as:

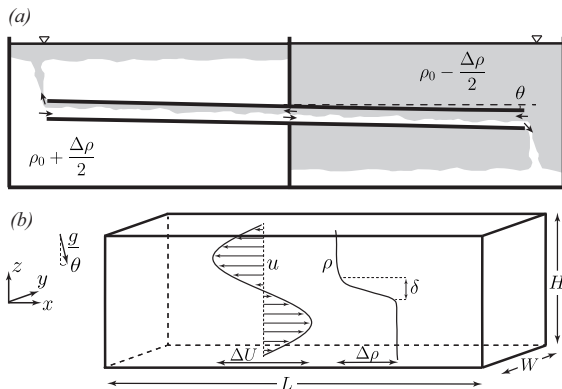


Figure 1: (a) The Stratified Inclined Duct (SID), in which an exchange flow takes place through a rectangular duct connecting two reservoirs at densities $\rho_0 \pm \Delta\rho/2$ and inclined at an angle θ from the horizontal. (b) Notation (in dimensional units). The x and z axes are respectively aligned with the horizontal and vertical of the duct (hence $-z$ makes an angle θ with gravity, here $\theta > 0$). The duct has dimensions $L \times W \times H$. The streamwise velocity u has typical peak-to-peak magnitude ΔU . The density stratification ρ has magnitude $\Delta\rho$, with an interfacial layer of typical thickness δ .

91 interfacial ‘Holmboe’ waves (Salehipour *et al.* 2016; Lefaue *et al.* 2018); spatio-temporal
 92 turbulent intermittency (de Bruyn Kops 2015; Portwood *et al.* 2016; Taylor *et al.* 2016);
 93 and layering and mixing (Salehipour & Peltier 2015; Zhou *et al.* 2017; Lucas *et al.* 2017;
 94 Salehipour *et al.* 2018).

95 To achieve this aim, the remainder of the paper is organised as follows. In § 2 we
 96 introduce a canonical experiment ideally suited to study the rich dynamics of exchange
 97 flows, and analyse the *a priori* importance of its non-dimensional input parameters. In
 98 § 3 we review the current state of knowledge on the behaviour of our three key variables
 99 in order to motivate our study. In § 4 we present our experimental results and scaling
 100 laws. In § 5 we explain some of these results with a variety of models, and we summarise
 101 and conclude in § 6.

102 2. The experiment

103

2.1. Setup and notation

104

The stratified inclined duct experiment (hereafter abbreviated ‘SID’) is sketched in
 105 figure 1(a). This conceptually simple experiment consists of two reservoirs initially filled
 106 with aqueous solutions of different densities $\rho_0 \pm \Delta\rho/2$, connected by a long rectangular
 107 duct that can be tilted at an angle θ from the horizontal. At the start of the experiment,
 108 the duct is opened, initiating a brief transient gravity current. Shortly after, at $t = 0$,
 109 an exchange flow starts and is sustained through the duct for long periods of time, until
 110 the accumulation of fluid of a different density from the other reservoir reaches the ends
 111 of the duct and the experiment is stopped at $t = T$ (typically after several minutes and
 112 many duct transit times). This exchange flow has at least four qualitatively different flow
 113 regimes, based on the experimental input parameters, as we discuss later in the paper.

114

Our notation is shown in figure 1(b) and largely follows that of Lefaue *et al.* (2018,
 115 2019). The duct has length L , height H , and width W . The streamwise x axis is aligned
 116 along the duct and the spanwise y axis is aligned across the duct, making the z axis tilted

at an angle θ from the vertical (resulting in a non-zero streamwise projection of gravity $g \sin \theta$). The angle θ is defined to be positive when the bottom end of the duct sits in the reservoir of lower density, as shown here. The velocity vector field is $\mathbf{u}(x, y, z, t) = (u, v, w)$ along x, y, z , and the density field is $\rho(x, y, z, t)$. All spatial coordinates are centred in the middle of the duct, such that $(x, y, z, t) \in [-L/2, L/2] \times [-W/2, W/2] \times [-H/2, H/2] \times [0, T]$.

Next, we define two integral scalar quantities of particular interest in exchange flows:

- (i) Q the *volume flux* as the volumetric flow rate averaged over the duration of an experiment

$$Q \equiv \langle |u| \rangle_{x,y,z,t}, \quad (2.1)$$

where $\langle |u| \rangle_{x,y,z,t} \equiv 1/(LWHT) \int_0^T \int_{-H/2}^{H/2} \int_{-W/2}^{W/2} \int_{-L/2}^{L/2} |u| dx dy dz dt$. The volume flux $Q > 0$ measures the magnitude of the exchange flow between the two reservoirs. It is different from the *net* (or ‘barotropic’) volume flux $\langle u \rangle_{x,y,z,t} \approx 0$, since, to a good approximation, the volume of fluid in each reservoir is conserved during an experiment (assuming the levels of the free surface in each reservoir are carefully set before the start of the experiment).

- (ii) Q_m the *mass flux* as the net flow rate of mass averaged of the duration of an experiment

$$Q_m \equiv \frac{2}{\Delta\rho} \langle (\rho - \rho_0)u \rangle_{x,y,z,t}, \quad (2.2)$$

which is equivalent to a *buoyancy flux* up to a multiplicative constant g . By definition $0 < Q_m \leq Q$. The first inequality holds since, in our notation, negatively-buoyant fluid ($\rho_0 < \rho \leq \rho_0 + \Delta\rho/2$) flows on average to the right ($u > 0$) and conversely. The second inequality would be an equality in the absence of molecular diffusion inside the duct (i.e. if all fluid moving right had density $\rho_0 + \Delta\rho/2$ and conversely). In any real flow, laminar (and potentially turbulent) diffusion at the interface are responsible for an interfacial layer of intermediate density $|\rho - \rho_0| < \Delta\rho/2$ of finite thickness $\delta > 0$ (figure 1(b)).

2.2. Non-dimensionalisation

A total of seven parameters are believed to play important roles in the SID: four geometrical parameters: L, H, W, θ , and three dynamical parameters: the reduced gravity $g' \equiv g\Delta\rho/\rho_0$ (under the Boussinesq approximation $0 < \Delta\rho/\rho_0 \ll 1$), the kinematic viscosity of water ($\nu = 1.05 \times 10^{-6} \text{ m}^2 \text{ s}^{-1}$) and the molecular diffusivity of the stratifying agent (active scalar) κ . In this paper, we will primarily consider salt stratification ($\kappa_S = 1.50 \times 10^{-9} \text{ m}^2 \text{ s}^{-1}$), but will also discuss temperature stratification ($\kappa_T = 1.50 \times 10^{-7} \text{ m}^2 \text{ s}^{-1}$). From these seven parameters having two dimensions (of length and time), we construct five independent non-dimensional parameters below.

The first three non-dimensional parameters are geometrical: θ , and the aspect ratios of the duct in the longitudinal and spanwise direction, respectively:

$$A \equiv \frac{L}{H} \quad \text{and} \quad B \equiv \frac{W}{H}, \quad (2.3)$$

We choose to non-dimensionalise lengths by the length scale $H/2$, defining the non-dimensional position vector as $\tilde{\mathbf{x}} \equiv \mathbf{x}/(H/2)$ such that $(\tilde{x}, \tilde{y}, \tilde{z}) \in [-A, A] \times [-B, B] \times [-1, 1]$. As an exception, we choose to non-dimensionalise the typical thickness of the interfacial density layer by H , for consistency with other definitions in the literature on mixing in exchange flows: $\tilde{\delta} \equiv \delta/H$, such that $\tilde{\delta} \in [0, 1]$.

158 The last two non-dimensional parameters are dynamical. We define an ‘input’ Reynolds
159 number based on the velocity scale $\sqrt{g'H}$ and length scale $H/2$:

$$Re \equiv \frac{\sqrt{g'H}H}{2\nu} = \frac{\sqrt{gH^3}}{2\nu} \sqrt{\frac{\Delta\rho}{\rho_0}}. \quad (2.4)$$

160 Consequently, we non-dimensionalise the velocity vector as $\tilde{\mathbf{u}} \equiv \mathbf{u}/\sqrt{g'H}$, and time by
161 the advective time unit $\tilde{t} \equiv 2\sqrt{g'H}/t$ (hereafter abbreviated ATU). We define our last
162 parameter, the Prandtl number (or Schmidt number), as the ratio of the momentum to
163 active scalar diffusivity:

$$Pr \equiv \frac{\nu}{\kappa}. \quad (2.5)$$

164 where κ takes the value κ_S or κ_T depending on the type of stratification (salt or
165 temperature, giving respectively $Pr = 700$ and $Pr = 7$). Finally, we define the non-
166 dimensional Boussinesq density field as $\tilde{\rho} \equiv (\rho - \rho_0)/(\Delta\rho/2)$, such that $\tilde{\rho} \in [-1, 1]$.

167 We now reformulate the aim of this paper (introduced in § 1) more specifically as:
168 exploring the behaviour of flow regimes, mass flux \tilde{Q}_m , and interfacial layer thickness $\tilde{\delta}$
169 in the five-dimensional space of non-dimensional input parameters (A, B, θ, Re, Pr) .

170 In the next section we address the dimensional scaling of the velocity in the experiment.
171 By discussing the *a priori* influence of the input parameters identified above on the
172 velocity scale in this problem, we will provide a basis for subsequent scaling arguments
173 in the paper.

174 2.3. Scaling of the velocity

175 Having constructed our Reynolds number (2.4) using the velocity scale $\sqrt{g'H}$, here
176 we show that it is the relevant velocity scale to use in such exchange flows. As sketched
177 in figure 1(b), we define the typical peak-to-peak velocity as ΔU . This velocity scale is
178 not set by the experimenter as an input parameter, rather it is chosen by the flow as an
179 output parameter. From dimensional analysis, we write

$$\frac{\Delta U}{2} = \sqrt{g'H} f_{\Delta U}(A, B, \theta, Re, Pr). \quad (2.6)$$

180 In order to show that our Reynolds number (2.4) and our non-dimensionalisation the
181 velocity by $\sqrt{g'H}$ are relevant (and such that $\tilde{u} \in [-1, 1]$), we will show below that
182 we indeed expect $\Delta U/2 \sim \sqrt{g'H}$ and $f_{\Delta U}(A, B, \theta, Re, Pr) \sim 1$. Although some aspects
183 of this discussion can be found in Lefauve *et al.* (2018, 2019), the importance of this
184 dimensional analysis for this paper justifies the more detailed discussion that we offer
185 below.

186 The velocity scale ΔU in quasi-steady state results from a dynamical balance in
187 the steady, horizontal momentum equation under the Boussinesq approximation (in
188 dimensional units)

$$\underbrace{\mathbf{u} \cdot \nabla \mathbf{u}}_{\text{inertial (I)}} = - \underbrace{(1/\rho_0)\partial_x p}_{\text{hydrostatic (H)}} + \underbrace{g \sin \theta (\rho - \rho_0)/\rho_0}_{\text{gravitational (G)}} + \underbrace{\nu \nabla^2 \mathbf{u}}_{\text{viscous (V)}}, \quad (2.7)$$

189 In addition to the standard inertial (I) and viscous (V) terms, this equation highlights
190 the two distinct ‘forcing’ mechanisms in SID flows:

191 (H) a *hydrostatic* longitudinal pressure gradient, the minimal ingredient for exchange
192 flow, resulting from each end of the duct sitting in reservoirs at different densi-
193 ties. This hydrostatic pressure in the duct increases linearly with depth $\partial_x p =$

194 $g \cos \theta \Delta \rho / (4L)z$, driving a flow in opposite directions on either side of the neutral
 195 level $z = 0$: $-(1/\rho_0)\partial_x p = g' \cos \theta / (4L)z$;

196 (G) a *gravitational* body force reinforcing the flow by the the acceleration of the
 197 positively-buoyant layer upward (to the left in figure 1) and of the negatively-
 198 buoyant layer downward (to the right) when the tilt angle is positive $g \sin \theta > 0$
 199 (the focus of this paper), and conversely when the tilt angle is negative.

200 Rewriting (2.7) in non-dimensional form and ignoring multiplicative constants, we obtain

$$201 \underbrace{(\Delta U)^2 \tilde{\mathbf{u}} \cdot \tilde{\nabla} \tilde{\mathbf{u}}}_{\text{I}} \sim \underbrace{(g'H \cos \theta) \tilde{z}}_{\text{H}} + \underbrace{(g'L \sin \theta) \tilde{\rho}}_{\text{G}} + \underbrace{(\nu \Delta U \ell^{-2} L) \tilde{\nabla}^2 \tilde{\mathbf{u}}}_{\text{V}}, \quad (2.8)$$

202 where ℓ is the smallest length scale of density gradients ($\ell = \delta$ in laminar flows, and
 203 $\ell \ll \delta$ in turbulent flows).

204 To simplify this complex ‘four-way’ balance, it is instructive to consider the four
 205 possible ‘two-way’ dominant balances to deduce four possible scalings for ΔU (ignoring
 206 constants and assuming $\cos \theta \approx 1$ since the focus of this paper is on small angles).

207 (IH) *The inertial-hydrostatic balance.* First, we can neglect the gravitational (G) term
 208 with respect to the hydrostatic (H) term if $g'H \cos \theta \gg g'L \sin \theta$, i.e. when the tilt
 209 angle of the duct θ is much smaller than its ‘geometrical’ angle:

$$0 < \theta \ll \alpha \quad (2.9)$$

210 where we define the geometrical angle as

$$\alpha \equiv \tan^{-1}(A^{-1}) \quad (2.10)$$

211 Second, we can neglect the viscous (V) term if $g'H \gg \nu \Delta U \ell^{-2} L$, i.e. if the Reynolds
 212 number is larger than $Re \gg HL/\ell^2$. This corresponds to

$$Re \gg A \quad (2.11)$$

213 in laminar flow (ignoring the case $B \ll 1$ for simplicity), and to a larger lower
 214 bound in turbulent flows. Under these conditions, balancing I and H gives the
 215 scaling $\Delta U \sim \sqrt{g'H}$, i.e. $f_{\Delta U} \sim 1$, which corresponds to our choice in § 2.1.

216 (IG) *The inertial-gravitational balance.* Using analogous arguments, if $\theta \gg \alpha$ and $Re \gg$
 217 HL/ℓ^2 , we expect the scaling $\Delta U \sim \sqrt{g'L \sin \theta}$, i.e. $f_{\Delta U}(A, \theta) \sim \sqrt{A \sin \theta} \gg 1$.

218 (HV) *The hydrostatic-viscous balance.* If $\theta \ll \alpha$ and $Re \ll A$, we expect $f_{\Delta U}(A, B, Re) \sim$
 219 $A^{-1} Re \ll 1$ (some dependence on B being unavoidable in such a viscous flow).

220 (GV) *The gravitational-viscous balance.* If $\theta \gg \alpha$ and $Re \ll A$, we expect
 221 $f_{\Delta U}(B, \theta, Re) \sim \sin \theta Re \ll A$.

222 Figure 2 summarises the above analysis and the following conclusions.

223 (i) The parameters A , θ and Re play particularly important roles in SID flows, since
 224 the variation of θ and Re above or below thresholds set by A can alter the scaling
 225 of ΔU (i.e. $f_{\Delta U}$). The parameter B appears less important in this respect (except
 226 in narrow ducts where $B \ll 1$ and the Re threshold becomes AB^{-2}).

227 (ii) At low tilt angles $0 < \theta \ll \alpha$, $f_{\Delta U}$ increases from $\ll 1$ when $Re \ll A$ to ~ 1 when
 228 $Re \gg A$. At high enough Re , $f_{\Delta U}$ likely retains a dependence on A, B, Re due to
 229 turbulence (the constant ‘IH’ scaling being a singular limit for $Re \rightarrow \infty$).

230 (iii) At high tilt angles $\theta \gg \alpha$ and Reynolds number $Re \gg A$, $f_{\Delta U}$ *should* increase well

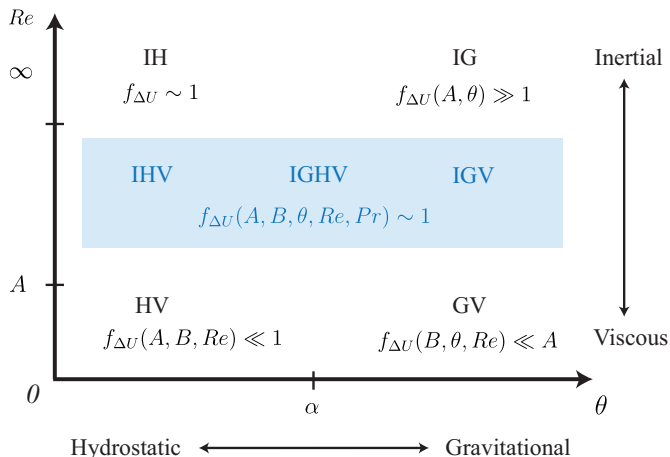


Figure 2: Summary of the scaling analysis of ΔU based on the four two-way dominant balances of the streamwise momentum equation (2.8). In each corner of the (θ, Re) plane, the IH, IG, HV, and GV balances predict the scaling of $f_{\Delta U} \equiv \Delta U / (2\sqrt{g'H})$ on either extreme side of $\theta = \alpha \equiv \tan^{-1}(A^{-1})$ and $Re = A$. The region of practical interest studied in this paper is shown in blue. Although no *a priori* ‘two-way’ balance allows us to determine accurately the scaling of $f_{\Delta U}(A, B, \theta, Re, Pr)$ in this region, hydraulic control requires that $f_{\Delta U} \sim 1$, as in the IH scaling (see text).

231 above 1, and likely retains a dependence on A, B, θ, Re (the ‘IG’ scaling being a
232 singular limit for $Re \rightarrow \infty$).

233 (iv) The blue rectangle in figure 2 represents the region of interest in most exchange flows
234 of practical interest and in this paper. In this region, three or four physical mecha-
235 nisms must be considered simultaneously (IHV, IGHV or IGV). Since few flows ever
236 satisfy $\theta \ll \alpha$ or $\gg \alpha$, we consider that in general $f_{\Delta U} = f_{\Delta U}(A, B, \theta, Re, Pr)$ (the
237 Pr dependence reflects the fact that the active scalar can no longer be neglected at
238 high Re due to its effect on turbulence and mixing). The existence and value of the
239 upper edge of this region, i.e. the Re value at which viscous and diffusive effects are
240 negligible (the ‘practical $Re = \infty$ limit’) are *a priori* unknown.

241 Although the above ‘two-way’ balances do not allow us to confidently guess the scaling
242 of $f_{\Delta U}$ in the blue region, theoretical arguments and empirical evidence of *hydraulic*
243 *control* support $f_{\Delta U}(A, B, \theta, Re, Pr) \sim 1$ for IHV, IGHV and IGV flows.

244 Hydraulic control of two-layer exchange flows dates back to Stommel & Farmer (1953);
245 Wood (1968, 1970) and was formalised mathematically by Armi (1986); Lawrence (1990);
246 Dalziel (1991). In steady, inviscid, irrotational, hydrostatic (i.e. ‘IH’) exchange flows, the
247 ‘composite Froude number’ G is unity, which using our notation and assuming streamwise
248 invariance of the flow ($\partial_x = 0$), reads:

$$G^2 = 4 \frac{\langle u^2 \rangle_{x,y,z,t}}{\sqrt{g'H}} = 1 \implies \langle |\tilde{u}| \rangle_{x,y,z,t} = \tilde{Q} = \frac{1}{2}. \quad (2.12)$$

249 Such exchange flows are called *maximal*: the phase speed of long interfacial gravity waves
250 $\sqrt{g'H}$ ‘controls’ the flow at sharp changes in geometry (on either ends of the duct), and
251 sets the maximal non-dimensional volume flux to $\tilde{Q} = 1/2$.

252 In ‘plug-like’ hydraulic flows ($Re \rightarrow \infty$), the velocity in each layer $\Delta U/2$ is equal to
253 its layer-average Q , giving an upper bound $f_{\Delta U} = \tilde{Q} = 1/2$. By contrast, in real-life

finite- Re flows, the peak $\Delta U/2$ is larger than the average Q (typically by a factor ≈ 2), such that the upper bound is $f_{\Delta U} \approx 2\tilde{Q} \approx 1$. This upper bound remains approximately valid throughout the blue region of figure 2. We thus answer the question motivating this section: our choice of non-dimensionalising \mathbf{u} by $\sqrt{g'H} \approx \Delta U/2$ in order to have $|\tilde{\mathbf{u}}| \lesssim 1$ is indeed relevant to SID flows.

Henceforth, we drop the tildes and, unless explicitly stated otherwise, use non-dimensional variables throughout.

3. Background

We sketch the current state of knowledge on the behaviour of flow regimes, mass flux, and interfacial layer thickness with input parameters in § 3.1. We highlight the limitations of previous studies and the current open questions to motivate our study in § 3.2. A more thorough review of the literature supporting these conclusions is given in appendix A, and a synthesis is given in table A.1.

3.1. Current state of knowledge

The flow regimes have been observed and classified in a relatively consistent way in the literature. Throughout this paper, we adopt the nomenclature of Meyer & Linden (2014): L (laminar flow with flat interface) H (interfacial Holmboe waves), I (intermittently turbulent), T (fully turbulent). The consensus is that the flow becomes increasingly disorganised and turbulent with A , θ and Re . At a fixed $\theta \geq 0^\circ$, all flow regimes (L, H, I, T) can be visited by increasing Re , and conversely at fixed Re and increasing θ (Macagno & Rouse 1961; Wilkinson 1986; Kiel 1991; Meyer & Linden 2014; Lefauve *et al.* 2019) (hereafter MR61, W86, K91, ML14 and LPL19, respectively). Both K91 and ML14 observed regime transitions scaling with $A \tan \theta = \tan \theta / \tan \alpha$ (or $A\theta$ for small angles), i.e. A controls the θ scaling. However, the scaling in Re is subject to debate, and may change on either side of $\theta \approx \alpha$ (LPL19). These conclusions are illustrated schematically in figure 3(a) (the interrogation marks denote open questions).

The mass flux has a complex non-monotonic behaviour in A, θ, Re sketched in figure 3(b). While the dependence on Re is clear at $Re < 500A$ (MR61, W86, ML14, LPL19) due to the influence of viscous boundary layers, it is still debated at $Re > 500A$: Mercer & Thompson (1975) (hereafter MT75) and ML14 argued in favour of this dependence on Re even above $500A$ whereas Leach & Thompson (1975) (hereafter LT75) and K91 argued against it. The mass flux reaches a maximum $Q_m \approx 0.4 - 0.5$ at $\theta \approx \alpha/2$ and ‘high enough’ Re (MT75, K91, ML14, LPL19) and decays for smaller/larger θ and Re (W86, LPL19) in a poorly-studied fashion.

The interfacial layer thickness has only been studied experimentally in K91, who observed monotonic increase of δ with both A and θ , good collapse with $A \tan \theta$ (reaching its maximum $\delta = 1$ at $\theta \gtrsim 2\alpha$), and independence on Re (figure 3(c)). The behaviour of δ at low $Re < 500A$ remains unknown.

3.2. Limitations of previous studies

Many aspects of the scaling of regimes, Q_m and δ with A, B, θ, Re, Pr remain open questions. For example, the effects of Re on δ , and the effects of B and Pr on all three variables have not been studied at all. Moreover, despite our efforts to unify their findings in § 3.1 and appendix A, these past studies of the SID experiment inherently provide a fragmented view of the problem due to the following limitations (made clear by table A.1):

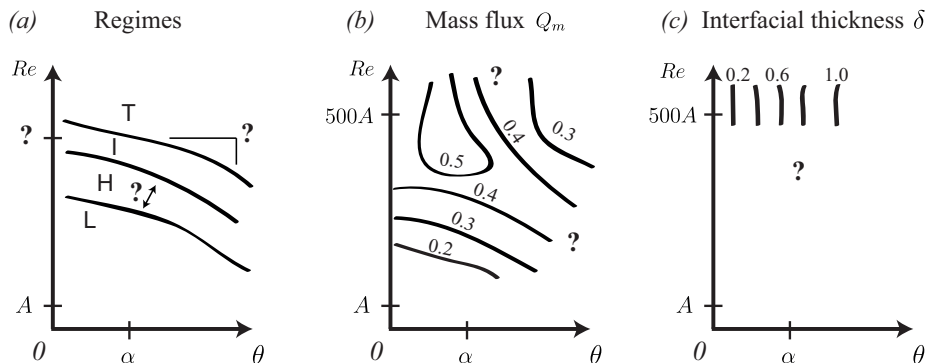


Figure 3: Illustration of the current state of knowledge on the idealised behaviour of the (a) flow regimes, (b) mass flux, and (c) interfacial layer thickness with respect to A, θ, Re (the axes have logarithmic scale). Interrogation marks refer to open questions. For more details, see the literature review in appendix A.

- 299 (i) they used slightly different setups and geometries (e.g. presence *vs* absence of free
 300 surfaces in the reservoirs, rectangular ducts *vs* circular pipes), and slightly different
 301 measuring methodologies (e.g. for Q_m);
- 302 (ii) only one study (K91) addressed the interdependence of the three variables of interest
 303 (regime, Q_m, δ), while the remaining studies measured either only regimes (MR61),
 304 only Q_m (LT75, MT75), or both (ML14, LPL19);
- 305 (iii) they focused on the variation of a single parameter (MR61), two parameters (W86,
 306 K91, LPL19), or at most three parameters (MT75, ML14) in which case the third
 307 parameter took only two different values;
- 308 (iv) they studied limited regions of the parameter space, and it is difficult to confidently
 309 interpolate results obtained by different setups in different regions (such as $Re <$
 310 $500A$ and $> 500A$).

311 The experimental results and models in the next two sections attempt to overcome the
 312 above limitations by providing a more unified view of the problem.

313 4. Experimental results

314 In order to make progress on the scaling of flow regimes, Q_m and δ with A, B, θ, Re, Pr ,
 315 we obtained a comprehensive set of experimental data using an identical setup, measuring
 316 all three dependent variables with the same methodology (described in appendix B),
 317 and varying all five independent parameters in a systematic fashion. We introduce the
 318 different duct geometries and data sets used in § 4.1, and present our results on flow
 319 regimes in § 4.2, on mass flux in § 4.3, and on interfacial layer thickness in § 4.4.

320

4.1. Data sets

321 All experimental data presented in the following were obtained in the stratified inclined
 322 duct (SID) setup sketched in figure 1. We used four different duct geometries and two
 323 types of stratification (salt and temperature) to obtain the following five distinct data
 324 sets, listed in table 1:

325 LSID (L for Large) with height $H = 100$ mm, and $A = 30, B = 1$;

Table 1: The five data sets used in this paper, using four duct geometries (abbreviated LSID, HSID, mSID, tSID) with different dimensional heights H , lengths $L = AH$ and widths $W = BH$, and two types of stratification (salt and temperature). We emphasise in bold the resulting differences in the ‘fixed’ non-dimensional parameters A, B, Pr with respect to the ‘control’ geometry (top row). We also emphasise the difference in H between LSID and mSID, to test whether or not H plays a role other than through the non-dimensional parameters A, B, Re . We also list the range of θ, Re explored, and the number of regime, Q_m and δ data points obtained in the (θ, Re) plane. Some of these data have been published or discussed in some form in ML14 (denoted by *) and LPL19 (denoted by †) and are reused here with their permission for further analysis. Measurements of Q_m and δ were not practical with heat stratification (hence the - symbol, see text for more details). Total: 886 individual experiments and 1545 data points.

| Name | Duct scale | | Fixed params. | | | Varied params. | | Number of data points | | |
|-------|------------|---|---------------|---------------|----------|-----------------------|------------------------|-----------------------|-------|----------|
| | H (mm) | Cross-section | A | B | Pr | θ ($^\circ$) | Re ($\times 10^3$) | regime | Q_m | δ |
| LSID | 100 |  | 30 | 1 | 700 | $[-1, 4]$ | $[2, 20]$ | 173* | 20* | 115 |
| HSID | 100 |  | 15 | 1 | 700 | $[0, 4]$ | $[1, 20]$ | 74* | 34* | 58 |
| mSID | 45 |  | 30 | 1 | 700 | $[-1, 6]$ | $[0.3, 6]$ | 360† | 162† | 91 |
| tSID | 90 |  | 15 | $\frac{1}{4}$ | 700 | $[-1, 3]$ | $[3, 15]$ | 131 | 92 | 87 |
| mSIDT | 45 |  | 30 | 1 | 7 | $[0, 10]$ | $[0.3, 1.5]$ | 148 | - | - |

326 HSID (H for Half) which only differs from the LSID (the ‘control’ geometry) in that
 327 it is half the length: $A = 15$ (highlighted in bold in table 1);

328 mSID (m for mini) which only differs from the LSID in its height $H = 45$ mm, but
 329 keeps A, B, Pr identical (this is done by scaling down H, W, L by the same factor
 330 $100/45$ such that the mSID and LSID ducts remain geometrically similar). Note
 331 that the mSID and LSID configurations *should* yield identical data at identical
 332 Re since H *should* only play a role through the non-dimensional parameters
 333 A, B, Re . However, we will see in § 4.2-4.4 that this hypothesis is challenged by
 334 our data.

335 tSID (t for tall) which differs from the HSID primarily in its tall spanwise aspect ratio
 336 $B = \frac{1}{4}$ (and, secondarily, in a marginally smaller height $H = 90$ mm);

337 mSIDT (m for mini and T for temperature) which differs from the mSID in that the
 338 stratification was achieved by different reservoir water temperatures (hence
 339 $Pr = 7$), as opposed to different salinities in the above data sets (where
 340 $Pr = 700$). This limited the density difference $\Delta\rho$ achieved, reflected in the
 341 lower Re .

Table 1 also lists, for each data set, the range of variation of θ and Re , and the number of data points, i.e. distinct (θ, Re) couples for which we have data on regime, Q_m , and δ .

Note that the regime and Q_m data of the top three data sets have already been published in some form by Meyer & Linden (2014) (ML14, denoted by *) and Lefauve *et al.* (2019) (LPL19, denoted by †), as discussed in Appendix A.1-A.2. However, ML14 plotted their LSID and HSID data together (see their figure 7-8) and did not investigate their potential differences, while LPL19 only commented in passing on a fit of the Q_m data in the (θ, Re) plane (see their figure 9). The individual reproduction and thorough discussion of these data alongside more recent data using a unified non-dimensional approach will be key to this paper. All five data sets have been used in the PhD thesis of Lefauve (2018) (especially in Chapters 3 and 5), and the detailed parameters of all experiments are tabulated in his appendix A for completeness. Most of the raw and processed data used in this paper are available on the repository doi.org/10.17863/CAM.48821 (more details in Appendix B).

Our focus on *long ducts*, evidenced by our choice of $A = 15$ and 30 , reflects our focus on flows relevant to geophysical and environmental applications, which are typically largely horizontal ($\theta \approx 0^\circ$) and stably stratified in the vertical (as opposed to the different case of vertical exchange flow with $\theta = 90^\circ$). The SID experiment conveniently exhibits all possible flow regimes, including high levels of turbulence and mixing, between $\theta = 0^\circ$ and a few α at most (§ 3.1). In long ducts (large A), $\alpha \equiv \tan^{-1}(A^{-1})$ is therefore small enough to allow us to study all the key dynamics of sustained stratified flows while keeping θ small enough for these flows to remain largely horizontal, and thus geophysically relevant.

As a result of this focus on long ducts, in the remainder of the paper we make the approximation that

$$\cos \theta \approx 1 \quad \text{and} \quad \sin \theta \approx \theta, \quad (4.1)$$

This approximation is accurate to better than 2 % for the angles considered in our data sets ($\theta \leq 10^\circ$). Unless explicitly specified by the $^\circ$ symbol, θ will now be expressed in radians (typically in scaling laws).

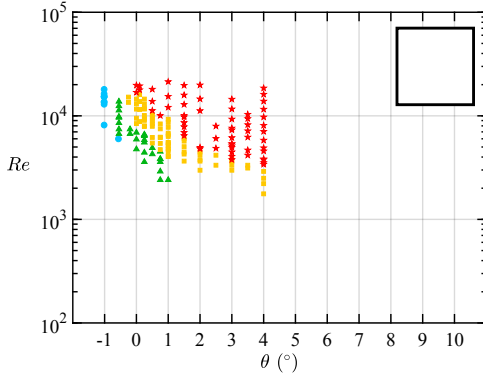
4.2. Flow regimes

The L, H, I, T flow regimes were determined following the ML14 nomenclature as in appendix B.1 (except for a new regime which we discuss in the next paragraph). Figure 4 shows the resulting regime maps in the (θ, Re) plane corresponding to the five data sets.

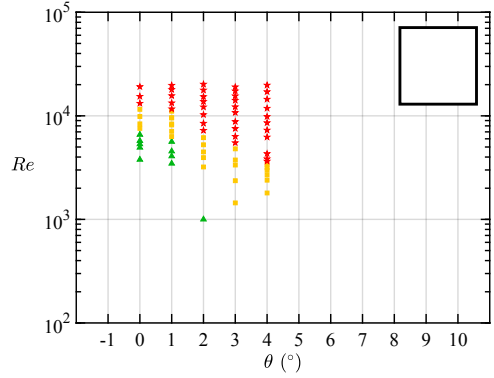
First, we note the introduction of a ‘new’ W regime in the tSID and mSIDT data (panels (d, e)). This W (wave) regime is similar to the H (Holmboe) regime, but describes interfacial waves which were not recognised as Holmboe waves in shadowgraphs. These waves were of two types. First, in the tSID geometry at positive angles $\theta > 0$, the waves did not exhibit the distinctive ‘cusped’ shape of Holmboe waves and the waves appeared to be generated at the ends of the duct and to decay as they travel inside the duct. Second, in the mSIDT larger-amplitude, tilde-shaped internal waves were observed across most of the height of the duct, contrary to Holmboe waves which are typically confined to a much thinner interfacial region. Further discussion of these waves falls outside the scope of this paper, but can be found in (Lefauve 2018, §§ 3.2.3-3.2.4) (hereafter abbreviated L18). This new observation highlights the richness of the flow dynamics in the SID experiment. However, for the purpose of this paper, the H and W regimes are sufficiently similar in their characteristics (mostly laminar flow with interfacial waves) that we group them under the same regime for the purpose of discussing regime transitions.

The main observation of figure 4 is that the transitions between regimes can be described as simple curves in the (θ, Re) plane that do not overlap (or ‘collapse’) between

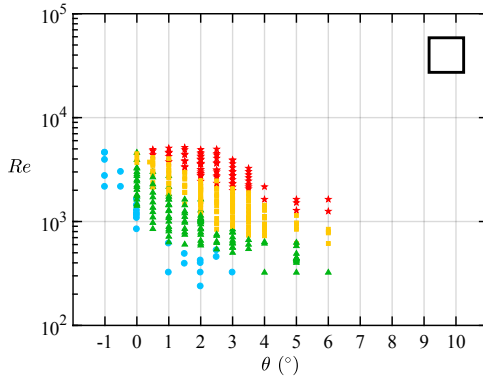
(a) LSID



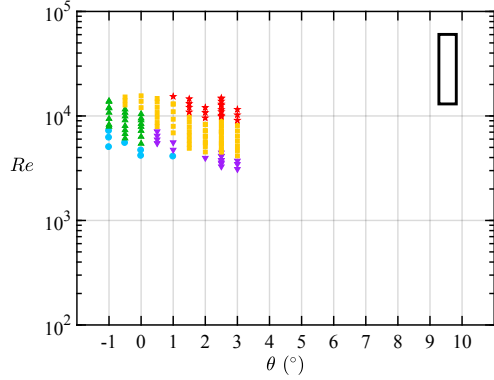
(b) HSID



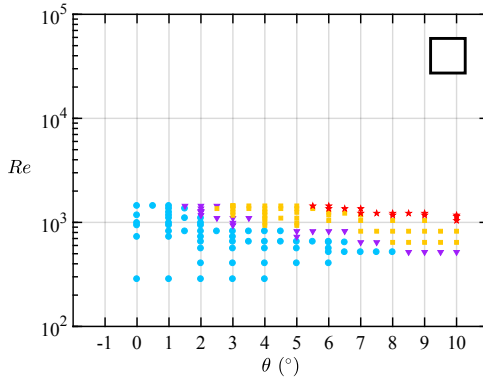
(c) mSID



(d) tSID



(e) mSIDT



• L
 ▼ W
 ▲ H
 ■ I
 ★ T

Figure 4: Regime diagrams in the (θ, Re) plane (lin-log scale) using the five data sets of table 1 (the scaled cross-section of each duct is sketched for comparison in the top right corner of each panel). The error in θ is of order $\pm 0.2^\circ$ and is slightly larger than the symbol size, whereas the error in Re is much smaller than the symbol size, except in (e) at small Re .

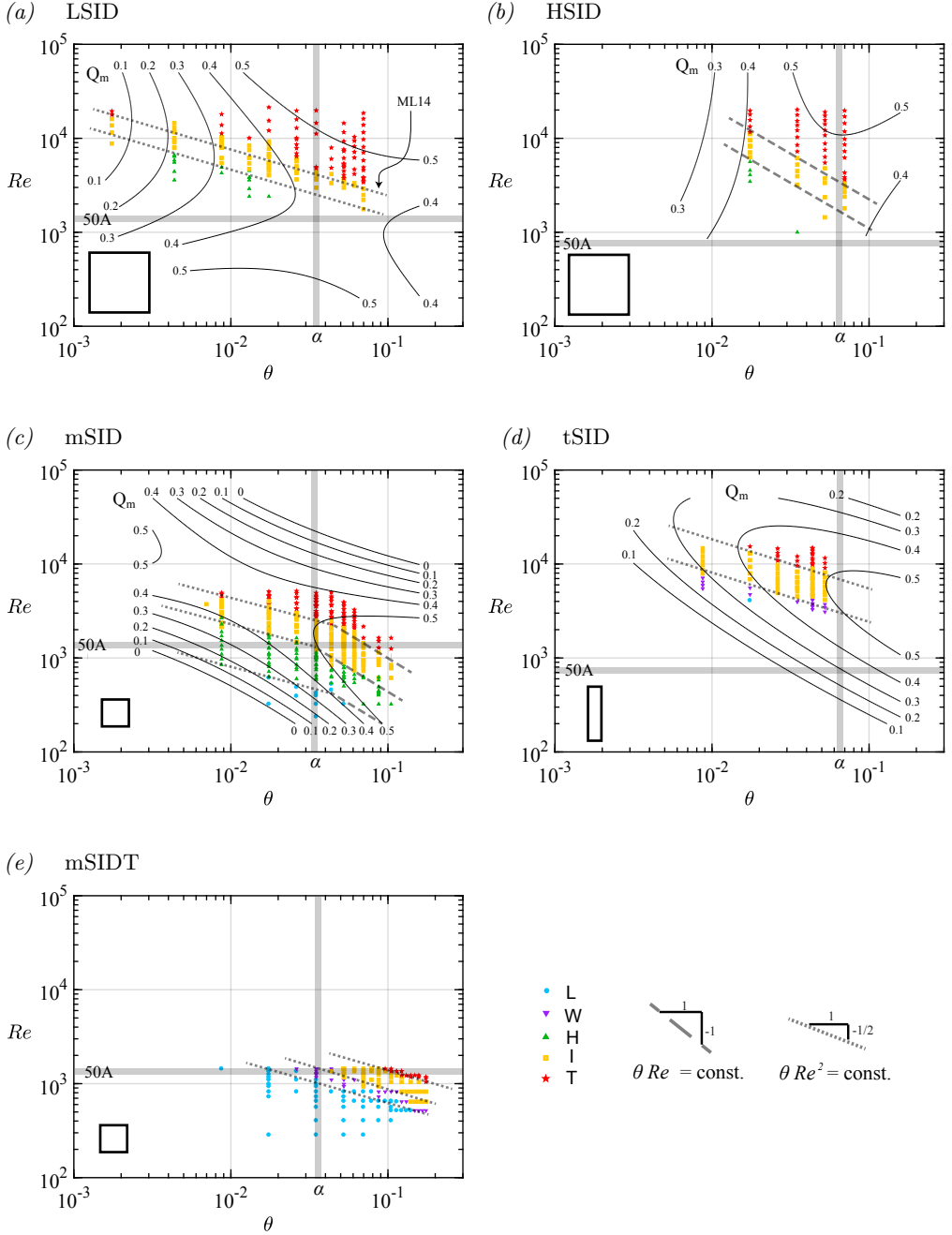


Figure 5: Regime and Q_m in the (θ, Re) plane (log-log scale, thus only containing the regime and Q_m data of figure 4 for which $\theta > 0^\circ$). The dashed and dotted lines represent the power law scalings $\theta Re = \text{const.}$ and $\theta Re^2 = \text{const.}$, respectively. The gray shadings represent the special threshold values of interest $\theta = \alpha$ and $Re = 50A$. The ML14 arrow in panel (a) denotes the I \rightarrow T transition curve identified by ML14. Black contours in panels (a-d) represent the fit to the Q_m data (see § 4.3), representing (a) 20 data points (coefficient of determination $R^2 = 0.56$), (b) 34 points ($R^2 = 0.81$), (c) 162 points ($R^2 = 0.80$), and (d) 92 points ($R^2 = 0.86$)

the five data sets. The slope and location of the transitions varies greatly between panels: the difference between the LSID and HSID data (panels (a,b)) is due to A , the difference between the HSID and tSID data (panels (b,d)) is due to B , and the difference between the mSID and mSIDT data (panels (c,e)) is due to Pr .

However one of the most surprising differences is that between LSID and mSID data (panel (a,c)), due to the dimensional height of the duct H (already somewhat visible in LPL19, figure 2). It is reasonable to expect that this H -effect is responsible for the main differences between the LSID/HSID/tSID data and the mSID/mSIDT data. In other words, it appears that the dimensional H is the main reason why the LSID/HSID/tSID transitions curves lie well above those for mSID/mSIDT, i.e. the same transitions occur at higher Re for larger H . The factor of ≈ 2 quantifying this observation suggests that a Reynolds number built using a length scale identical in all data sets (rather than $H/2$) would better collapse the data. However, such a length scale is missing in our dimensional analysis (§ 2.2) because we are unable to think of an additional length scale (such as the thickness of the duct walls or the level of the free surfaces in the reservoirs) that could play a significant dynamical role in the SID experiment.

We conclude that the transitions between flow regimes can be described by hyper-surfaces depending on all five parameters A, B, θ, Re, Pr because their projections onto the (θ, Re) plane for different A, B, Pr do not overlap. This dependence of flow regimes on all five parameters is interesting because it was not immediately obvious from our dimensional analysis which concerned the scaling of the velocity $f_{\Delta U}$ alone (§ 2.3 and figure 2). Furthermore, the existence of another non-dimensional parameter involving H and a ‘missing’ length scale is a major result that could not be predicted by physical intuition, and which this paper unfortunately does not elucidate.

Let us now investigate in more detail the scaling of regime transitions with respect to θ and Re , for which we have much higher density of data than for A, B, Pr . In figure 5, we replot the $\theta > 0$ data of figure 4 using a log-log scale (each panel corresponding to the respective panel of figure 4). To guide the eye to the two main types of regime transition scalings observed in these data, we also plot two families of lines: dashed lines with a $\theta Re = \text{const.}$ scaling, and dotted lines with a $\theta Re^2 = \text{const.}$ scaling. We also show using grey shading special values of interest: $\theta = \alpha$ and $Re = 50A$. The former was highlighted as particularly relevant in our scaling analysis (§ 2.3) and literature review (§ 3.1), notably as the boundary between lazy and forced flows in LPL19 (appendix A). Although W86 and K91 quoted $Re = 500A$ as a threshold beyond which the effects of viscosity should be negligible on the turbulence in the SID, we believe that $Re = 50A$ is a physically justifiable threshold beyond which the influence of the top and bottom walls of the duct becomes negligible. In the absence of turbulent diffusion, laminar flow in the duct is significantly affected by the top and bottom walls if the interfacial and wall 99 % boundary layers overlap in the centre of the duct ($x = 0$), which occurs for $Re < 50$ (L18, § 5.2.3). If, on the other hand, $Re \gg 50A$ ($Re = 500A$ being a potential threshold), the top and bottom wall laminar boundary layers (as well as the side wall laminar boundary layers, assuming that $B \ll 1$) do not penetrate deep into the ‘core’ of the flow (however at these Re , we expect interfacial turbulence to dominate the core of the flow). Note that black contours representing a fit of the Q_m data are superimposed in panels $(a-d)$; these will be discussed in § 4.3.

Figure 5 shows that regime transitions scale with $\theta Re^2 = \text{const.}$ (dotted lines) in LSID, tSID and mSIDT (panels (a,d,e)), and with $\theta Re = \text{const.}$ (dashed lines) in HSID (panel (b)). In mSID (panels (c)), these two different scalings coexist: θRe^2 for $\theta \lesssim \alpha$ (lazy flows) and θRe for $\theta \gtrsim \alpha$ (forced flows), as previously observed by LPL19, who physically substantiated the θRe scaling in forced flows, but not the θRe^2 scaling in lazy

flows. Furthermore, these five data sets show that this dichotomy in scalings between lazy and forced flows in mSID does not extend to all other geometries: lazy flows in the HSID exhibit a θRe scaling and forced flows in the mSIDT exhibit a θRe^2 scaling. These observations further highlight the complexity of the scaling of regime transitions with A, B, θ, Re, Pr .

4.3. Mass flux

Mass fluxes were determined using the same salt balance methodology as ML14 described in appendix B.2.

In figure 6 we plot the Q_m data for mSID (full symbols) and tSID (open symbols) as a function of Re for all the available θ (from $\theta = -1^\circ$ in panel (a) to $\theta = 3.5^\circ$ in panel (j)). The colour of each symbol denotes the regime as in figures 4-5 and the error bars denote the uncertainty about the precise duration T of the ‘steady’ flow of interest in an experiment (used to average the volume flux and obtain Q_m , as explained in appendix B.2). We do not plot the LSID and HSID data in this figure because they are sparser and do not have error bars (these data were collected by ML14 prior to this work).

At low angles $\theta \lesssim 1^\circ < \alpha$ (where $\alpha \approx 2^\circ$ in mSID and 4° in tSID) we observe low values $Q_m \approx 0.2 - 0.3$ in the L and H regimes. At intermediate angles $\theta \approx \alpha - 2\alpha$ we observe convergence to the hydraulic limit $Q_m \rightarrow 0.5$ (denoted by the dashed line), as discussed in § 2.3, which coincides with the I and T regimes. We also note that this hydraulic limit is not a strict upper bound in the sense that we observe values up to $Q_m = 0.6$ in some experiments (some error bars even going to 0.7). At higher angles $\theta \gtrsim \alpha \approx 2^\circ$, Q_m drops with Re while remaining fairly constant with θ .

As in the regime data, the mSID and tSID Q_m data do not collapse with Re : all the tSID data (open symbols) are shifted to larger Re compared to the mSID data (full symbols) suggesting again that a Reynolds number based on a ‘missing’ length scale independent of H would better collapse the data.

To gain more insight into the scaling of Q_m and its relation to the flow regimes, we superimpose on the regime data of figure 5(a-d) black contours representing the least-squares fit of our four Q_m data sets using the following quadratic form:

$$\begin{aligned}
 Q_m(\theta, Re) &= \Gamma_{00} + \Gamma_{10} \log \theta + \Gamma_{20} (\log \theta)^2 + \Gamma_{01} \log Re + \Gamma_{02} (\log Re)^2 + \Gamma_{11} \log \theta \log Re \\
 &= [\log \theta \quad \log Re \quad 1] \underbrace{\begin{bmatrix} \Gamma_{20} & \Gamma_{11}/2 & \Gamma_{10}/2 \\ \Gamma_{11}/2 & \Gamma_{02} & \Gamma_{01}/2 \\ \Gamma_{10}/2 & \Gamma_{01}/2 & \Gamma_{00} \end{bmatrix}}_{\mathbf{\Gamma}} \begin{bmatrix} \log \theta \\ \log Re \\ 1 \end{bmatrix}. \quad (4.2)
 \end{aligned}$$

This is the general equation of a conic section, where $\mathbf{\Gamma}$ is commonly referred to as the matrix of the quadratic equation. It is well suited to describe the non-monotonic behaviour observed above, despite the fact that the non-monotonicity in θ (i.e. the decay of Q_m at large θ widely observed in the literature) cannot be clearly confirmed by our data.

These contours describe hyperbolas ($\det \mathbf{\Gamma} < 0$) for LSID, HSID and mSID (panels (a,b,c)), and concentric ellipses ($\det \mathbf{\Gamma} > 0$) for tSID (panel (d)). The hydraulic limit $Q_m \approx 0.5$ is reached either at the saddle point of the hyperbolas (panels (a,b,c)), or at the centre of the ellipses (panels (d)), and, encouragingly, no $Q_m = 0.6$ contour exists here.

We again note that these four data sets do not collapse in the (θ, Re) plane. For example, the angle at which this maximum Q_m is achieved is a modest $\theta = 0.3\alpha$ in mSID

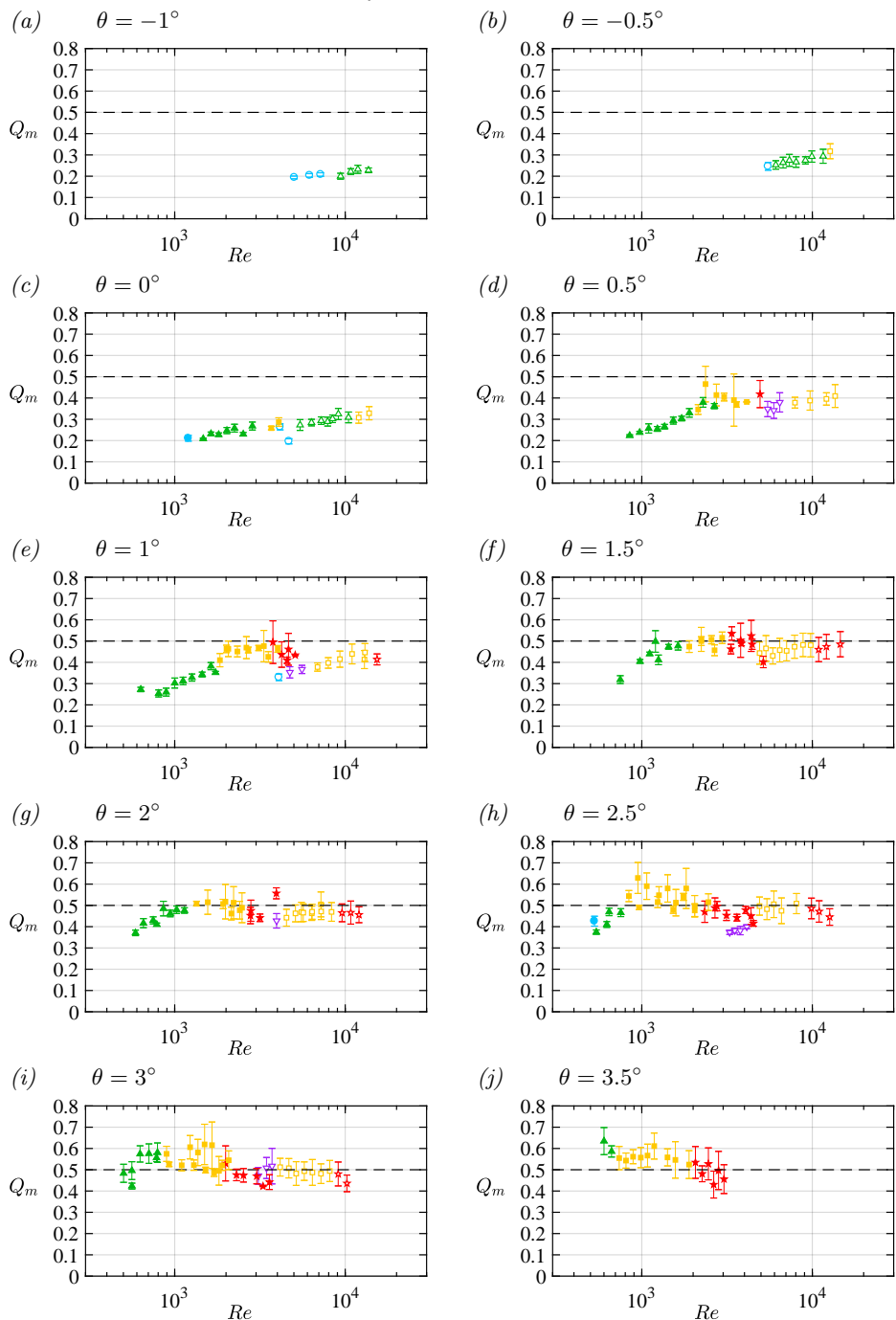


Figure 6: Mass flux for the mSID data set (full symbols) and tSID data set (open symbols) for as a function of Re for various $\theta \in [-1^\circ, 3.5^\circ]$ by 0.5° increments (a-j). The symbol colour denotes the regime as in figures 4 and 5. The mass flux Q_m is computed using the average estimation of the run time, and the error bars denote the uncertainty in this estimation (see appendix B.2).

481 (panel (c)) but appears much larger in tSID. The eigenvectors of \mathbf{T} for each data set reveal
 482 that the major axis of these conic sections has equation θRe^γ where $\gamma = 2.6, 0.3, 1.5, 1.2$
 483 respectively for panels (a, b, c, d) (a larger exponent γ represents a larger dependence on
 484 Re , hence a more horizontal axis).

485 The exponent γ characterising the slope of the major axis is roughly of the same
 486 order as the exponent characterising the lines of regime transition (which is 1 for the
 487 θRe scaling, and 2 for the θRe^2 scaling), suggesting that both phenomena (regime
 488 transition and non-monotonic behaviour of Q_m) are linked. However, this agreement
 489 is not quantitative except in mSID (panel (c)) where $\gamma = 1.5$ is precisely the average of
 490 the two different regime transition exponents. This general lack of correlation suggests
 491 that the relationship between regimes and Q_m in the SID is not straightforward and
 492 dependent on the geometry.

493 4.4. Interfacial layer thickness

494 Interfacial layer thickness was determined using the non-intrusive shadowgraph imag-
 495 ing technique (in salt experiments only). Shadowgraph is particularly suited to detect
 496 peaks in the vertical curvature of the density field $|\partial_{zz}\rho|$ which we define as the edges of
 497 the interfacial density layer, as explained in appendix B.3.

498 In figure 7 we plot δ for our four duct geometries (rows) and three particular angles
 499 (representing a subset of our data) $\theta = 1^\circ, 2^\circ, 3^\circ$ (columns). In figure 8 we plot a
 500 quadratic fit (black contours) to all the available data (represented by the symbols)
 501 in the $(\log \theta, \log Re)$ plane following (4.2). We also added in grey shading the $\theta = \alpha$ and
 502 $Re = 50A$ values of interest for comparison between panels. In both figures, the colour
 503 of the symbol denotes the flow regimes as in figures 4-6.

504 In figures 7 and 8, δ monotonically increases with both θ and Re , starting from values
 505 as low as $\delta \approx 0.05$ in the L, H, and W regimes (see figure B.1(a) for an illustration with
 506 $\delta = 0.069$), and ending with values as high as $\delta \approx 0.8$ in the T regime (see figure B.1(c)
 507 for an illustration with $\delta = 0.47$). The upper bound corresponds to the turbulent mixing
 508 layer filling 80 % of the duct height, with unmixed fluid only filling the remaining top
 509 and bottom 10 %. We substantiate the lower bound by the thickness of the 99 % laminar
 510 boundary layer resulting from the balance between streamwise advection and vertical
 511 diffusion of an initially step-like density field. This calculation gives, at any point in the
 512 duct, $\delta_{99} \approx 10A^{1/2}(Re Pr)^{-1/2} \approx 0.03 - 0.1$ in the range $Re \in [300, 6000]$ where the
 513 L, H, W regimes are found.

514 Figure 7 also shows a greater scatter of data points in the I and T regimes than in
 515 the L and H regime. This scatter cannot be attributed to measurement artifacts caused
 516 by turbulent fluctuations in the streamwise or spanwise position of the mixing layer
 517 (appendix B.3), but rather demonstrates the inherent physical variability and limited
 518 reproducibility of I and T flows.

519 Both figures show the role of the dimensional parameter H in ‘shifting’ the
 520 LSID/HSID/tSID data to higher Re than the mSID data and hindering their overlap,
 521 hinting at a ‘missing’ lengthscale, as already discussed in the regimes and Q_m data. Note
 522 that A and B play additional, more subtle roles as shown by the differences between the
 523 LSID and HSID data and between the HSID and tSID data, respectively.

524 Finally, figure 8 shows good agreement between iso- δ contours and ‘iso-regime’ curves,
 525 or regime transitions curves (not shown for clarity, but easily visualised by the different
 526 symbols). This suggests that δ is more closely correlated to regimes than Q_m is.

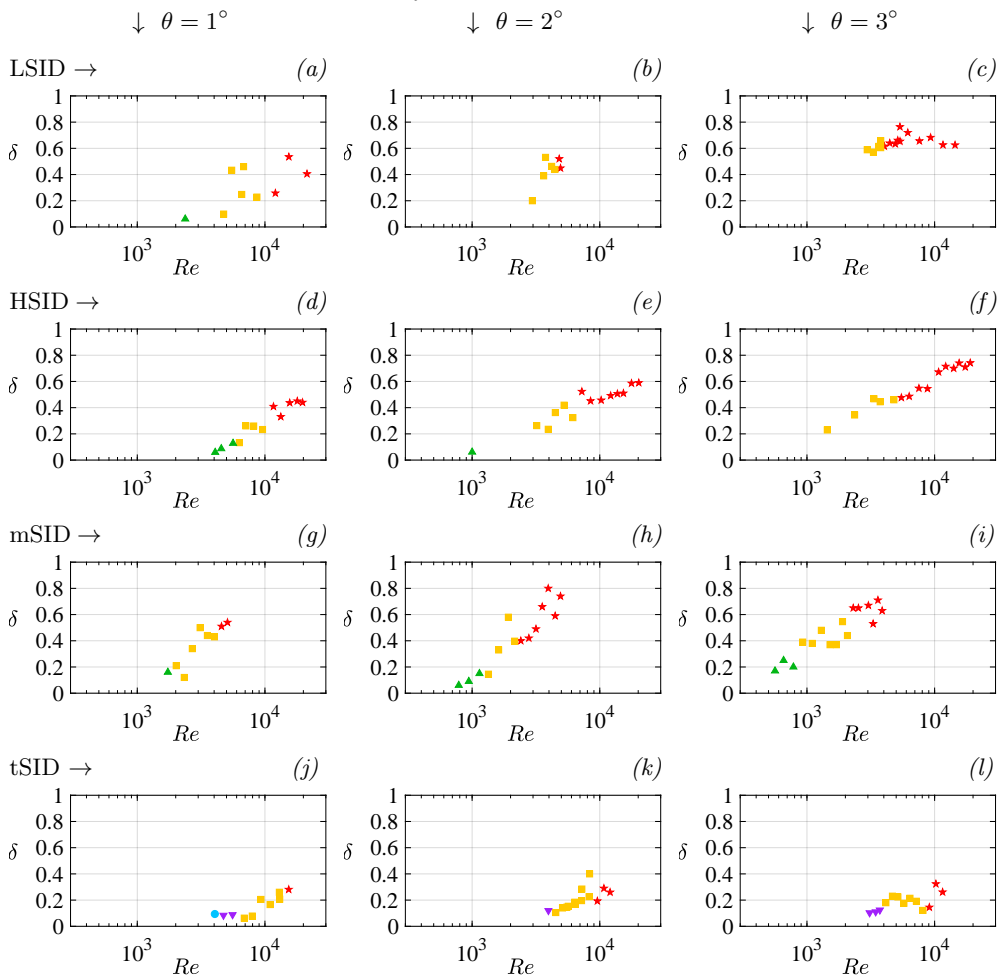


Figure 7: Interfacial density layer thickness $\delta(Re)$ in salt experiments for three selected angles $\theta = 1^\circ, 2^\circ, 3^\circ$ (only a fraction of the available data) and for the four duct geometries: (a-c) LSID, (d-f) HSID, (g-i) mSID, (j-l) tSID. Symbol colour denotes flow regime as in previous figures.

5. Models and discussion

In this section, we attempt to explain some of the above observations with three particular classes of models, whose prior success in the literature make them natural candidates to tackle this problem.

In § 5.1 we attempt to explain the scaling of regime transitions at high $Re \gg 50A$ by generalising the time- and volume-averaged energetics analysis of LPL19. In § 5.2, we investigate the scaling of regimes and Q_m with a frictional two-layer hydraulic model. In § 5.3, we tackle the scaling of δ in the I and T regimes by a variety of turbulence mixing models.

5.1. Volume-averaged energetics

The simultaneous volumetric measurements of the density and three-component velocity fields of Lefaue *et al.* (2019) (LPL19) confirmed their theoretical prediction that, in

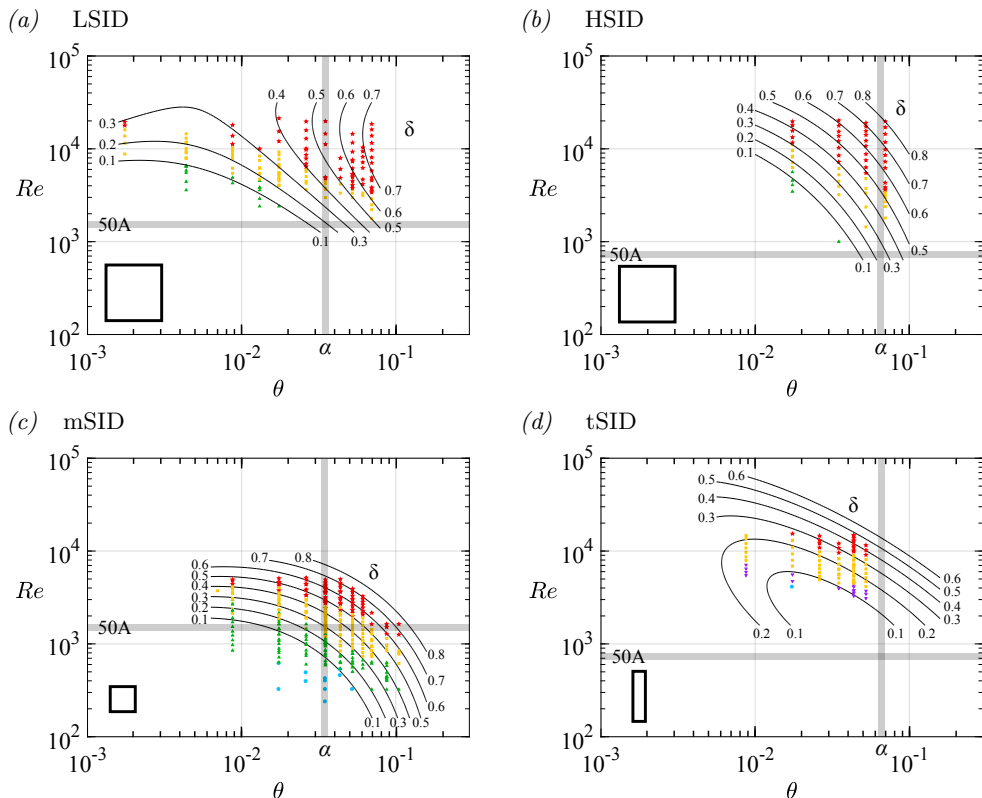


Figure 8: Interfacial density layer thickness δ in salt experiments fitted from (a) LSID: 115 points ($R^2 = 0.88$), (b) HSID: 58 data points ($R^2 = 0.97$), (c) mSID: 91 data points ($R^2 = 0.80$), (d) tSID: 87 data points ($R^2 = 0.75$). Symbol denotes location of the δ data and colour denotes flow regime. Grey shading denotes $\theta = \alpha$ and $Re = 50A$.

539 forced flows, ($\theta \gtrsim \alpha$) the time- and volume-averaged norm of the strain rate tensor (non-
 540 dimensional dissipation) followed the scaling $\langle s^2 \rangle_{x,y,z,t} \sim \theta Re$ (see § A.1 for a review).
 541 They further decomposed the dissipation into:

- 542 (i) a ‘two-dimensional’ component \mathbf{s}_{2d}^2 (based on the x -averaged velocity $\mathbf{u}_{2d} \equiv \langle \mathbf{u} \rangle_x$).
 543 LPL19 measured flows in the mSID geometry at $Re < 2500$, i.e. $Re \gg 50A = 1500$,
 544 in which case the viscous interfacial and top and bottom wall boundary layers are
 545 well or fully developed and $\mathbf{s}_{2d}^2 \sim \langle (\partial_z u_{2d})^2 \rangle_{x,y,z,t} = O(1)$. They indeed observed
 546 that $\langle \mathbf{s}_{2d}^2 \rangle_{x,y,z,t}$ plateaus at ≈ 4 in the I and T regimes due to the hydraulic limit;
- 547 (ii) a complementary ‘three-dimensional’ part $\mathbf{s}_{3d}^2 = \mathbf{s}^2 - \mathbf{s}_{2d}^2$ which, as a consequence of
 548 the plateau of \mathbf{s}_{2d}^2 , takes over in the I and T regime and explains the θRe scaling of
 549 regime transitions for forced flows in mSID.

550 In flows at $Re \gg 50A$ (well above the horizontal grey shading in figures 5, 8) we
 551 expect the 99 % viscous boundary layers to be of typical thickness $\sim 10A^{1/2}Re^{-1/2} \ll 1$,
 552 and therefore volume-averaged two-dimensional dissipation to be higher $\mathbf{s}_{2d}^2 \sim$
 553 $\langle (\partial_z u_{2d})^2 \rangle_{x,y,z,t} \sim 10^{-1}A^{-1/2}Re^{1/2} \gg 1$. Therefore, we extend the prior results of
 554 LPL19 that regime transitions correspond to threshold values of

$$\langle \mathbf{s}_{3d}^2 \rangle_{x,y,z,t} \sim \theta Re \quad \text{for } Re < 50A, \quad (5.1)$$

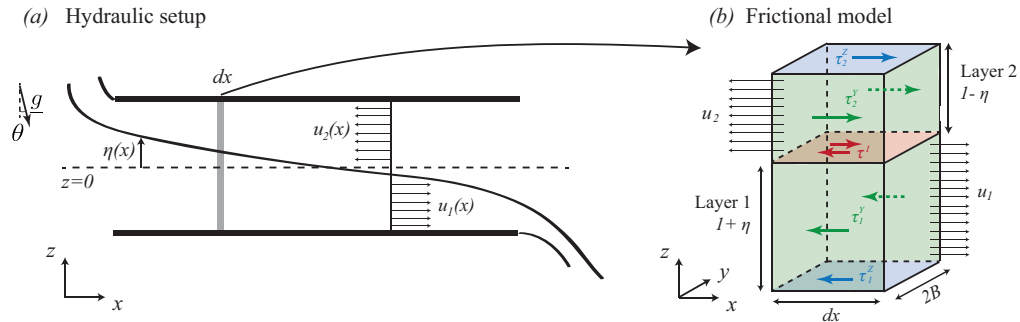


Figure 9: Schematics of the (a) hydraulic model setup and notation and (b) the frictional model with stresses acting on the: top and bottom walls $\tau_{1,2}^Z$ (in blue), side walls $\tau_{1,2}^Y$ (in green) and interface τ^I (in red) of an infinitesimally small slab of fluid dx .

555 by conjecturing that they correspond to threshold values of

$$\langle s_{3d}^2 \rangle_{x,y,z,t} \sim \theta Re - A^{-1/2} Re^{1/2} \quad \text{for } Re \gg 50A, \quad (5.2)$$

556 which introduces A and a different exponent to Re into the scaling.

557 Unfortunately we have little regime data for forced flows at $Re \gg 50A$ (upper right
558 quadrants of each panel in figure 5) except in LSID (panel (a)). Nevertheless, it does not
559 appear that this conjectured scaling would be able to explain the observed θRe^2 scaling.
560 Detailed flow measurements would be required in this geometry to confirm or disprove
561 the above two assumptions that two-dimensional dissipation follows a different scaling,
562 and that regime transitions are tightly linked to three-dimensional dissipation.

563 Furthermore, we recall that the under-determination of the energy budgets of lazy
564 flows ($\theta < \alpha$, see LPL19 figure 8(a)) does not allow us to predict the rate of energy
565 dissipation (s^2) from the rate of energy input ($\sim \theta Re$) and therefore to substantiate the
566 transition scalings in lazy flows (left two quadrants of each panel in figure 5).

5.2. Frictional two-layer hydraulics

567 We introduce the fundamentals of this model in § 5.2.1, before examining the physical
568 insight it provides in § 5.2.2, and its implications for the scaling of regime transitions
569 and mass flux in § 5.2.3.

5.2.1. Fundamentals

572 The two-layer hydraulic model for exchange flows (figure 9(a)) assumes two layers
573 flowing with non-dimensional velocities $u_1(x) > 0$ (lower layer) and $u_2(x) < 0$ (upper
574 layer), and separated by an interface of non-dimensional elevation $\eta(x) \in [-1, 1]$ above
575 the neutral level $z = 0$.

576 In the idealised *inviscid* hydraulic model (i.e. in the absence of viscous friction) the
577 conservation of volume and of Bernoulli potential, and the requirement of hydraulic
578 control yield a horizontal and symmetric interface $\eta(x) = 0$ for $x \in [-A, A]$ and a volume
579 flux $Q = u_1 = -u_2 = 1/2$ as already mentioned in § 2.3 (see appendix C.1 for more
580 details).

581 The *frictional* hydraulic model is of more relevance to SID flows at finite Re . This model
582 parameterises the effects of viscous friction while retaining the hydraulic assumptions
583 (hydrostatic, steady, two-layer flow with uniform velocities $u_{1,2}(x)$). Dating back to Schjif
584 & Schönfeld (1953); Assaf & Hecht (1974); Anati *et al.* (1977)), it was formalised by Zhu

585 & Lawrence (2000); Gu (2001); Gu & Lawrence (2005), who considered the effects of
 586 friction at the interface and bottom wall only, with applications to wide, open, horizontal
 587 channels. Here we further develop this model to add the effects of gravitational forcing
 588 ($\theta > 0$) and friction at the top and side walls. The full development of this model can
 589 be found in (L18, § 5.2) and we offer a summary in appendix C. Some of its conclusions
 590 were briefly discussed in LPL19 § 4.3.1 (e.g. the distinction between lazy/forced flows).
 591 Below we provide a self-contained presentation of the key results of this model regarding
 592 the particular problem of the scaling of regimes and Q_m .

593 As sketched in figure 9(b), we consider that each infinitesimal duct sub-volume $dx \times$
 594 $2B \times 2$ centred around x is subject to horizontal, resistive stresses at the bottom wall
 595 $\tau_1^Z(x)$, top wall $\tau_2^Z(x)$ (in blue), side walls $\tau_{1,2}^Y(x)$ (respectively in the bottom and top
 596 layers, in green), and interface τ^I (in red). The inclusion of these stresses in the evolution
 597 of Bernoulli potential along the duct (see § C.1) yields a nonlinear differential equation
 598 for the slope of the interface along the duct of the form

$$\eta'(x) = \eta'(\eta, Q, \theta, Re, f_Z, f_Y, f_I) \quad (5.3)$$

599 (see (C 24) for the full expression). Here f_Z, f_Y, f_I are constant friction factors parameter-
 600 ising respectively the top and bottom wall stress, the side wall stress, and the interfacial
 601 stress (they can be determined *a posteriori* from any finite- Re flow profile, see § C.2
 602 and (C 22)). For any set of parameters $\theta, Re, f_Z, f_Y, f_I$, this dynamical equation can be
 603 combined with the hydraulic control condition and solved numerically using an iterative
 604 method to yield a unique solution for Q and $\eta(x)$ (§ C.3). The volume flux Q generally
 605 increases with the forcing θRe , and decreases with friction f_Z, f_Y, f_I , and A .

606 5.2.2. Physical insight

607 We now consider the mid-duct slope $\eta'(x=0)$, whose simplified expression shows the
 608 balance between the forcing θRe and the ‘composite friction parameter’ F :

$$\eta'(0) = \frac{\theta Re - 2QF}{Re(1 - 4Q^2)} \quad \text{where} \quad F \equiv f_Z(1 + 2r_Y + 8r_I), \quad (5.4)$$

609 and $r_Y \equiv B^{-1}f_Y/f_Z$ and $r_I \equiv f_I/f_Z$ are respectively the side wall friction ratio and the
 610 interfacial friction ratio.

611 We further note that our model has three properties: (i) the interface must slope down
 612 everywhere ($\eta'(x) < 0$) since the lower layer accelerates convectively from left to right
 613 ($u_1 u_1'(x) > 0$) and conversely ($u_2 u_2'(x) < 0$); (ii) the interface must remain in the duct
 614 $|\eta(x = \pm A)| < 1$; (iii) η' always reaches a maximum ($|\eta'|$ reaches a minimum) at the
 615 inflection point $x = 0$.

616 From these properties we deduce that the existence of a solution requires the mid-duct
 617 interfacial slope to satisfy

$$-A^{-1} < \eta'(0) < 0, \quad (5.5)$$

618 and therefore, using (5.4), we obtain the following bounds:

$$\theta Re < 2QF < (1 + b)\theta Re \quad \text{where} \quad b(A, \theta, Q) \equiv \frac{1 - 4Q^2}{A\theta} \quad (5.6)$$

619 The first inequality in (5.5) comes from property (ii) and means that the mid-duct
 620 interfacial slope must not be too steep compared to the duct geometrical slope $A^{-1} \approx \alpha$.
 621 The second inequality comes from (i) and (iii) and means that the mid-duct interfacial
 622 slope must be negative for $\eta(x)$ to be negative everywhere.

623 When suitably rescaled by $2Q \in [0, 1]$, the combined friction parameter F must

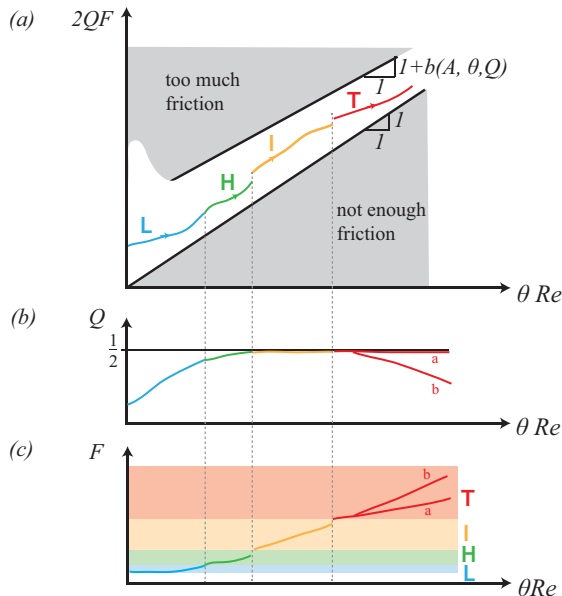


Figure 10: Conclusions of the frictional hydraulic model as the ‘forcing parameter’ θRe is increased: (a) $2QF$ is bounded above and below by (5.6); (b) volume flux Q , and (c) composite friction parameter F (a and b in the T regime denote two possible scenarios). We conjecture that regime transitions correspond to threshold values of F .

624 therefore follow a θRe scaling, strictly bounded from below. The upper bound in (5.6)
 625 is loose ($b > 0$) in lazy flows, and tight ($b \rightarrow 0$) in forced flows ($A\theta \approx \theta/\alpha \gg 1$ and
 626 $Q \rightarrow 1/2$).

627 5.2.3. Implications for regimes and Q_m

628 Combining the above physical insight with our experimental observations, we con-
 629 jecture the following behaviour about regimes and Q_m , summarised in figure 10.

- 630 (i) At zero or ‘low’ θRe (i.e. at $\theta \approx 0$, since Re must be large for hydraulic theory to
 631 hold) due to the inevitable presence of wall and interfacial friction ($F > 0$) and
 632 the looseness of the upper bound b , $2QF$ is typically well above the forcing θRe .
 633 The friction F is independent of θRe and the flow is typically laminar (L regime).
 634 The interface has a noticeable slope all along the duct $\eta'(0) \ll 0$, associated with a
 635 small volume flux $Q \ll 1/2$ (see (C 25)). Such *lazy flows* are underspecified, and the
 636 scaling of Q and F with θRe is therefore impossible to predict *a priori*.
- 637 (ii) At moderate θRe ($\theta > 0$): $2QF$ increases above its ‘default’ $\theta = 0$ value. This is
 638 achieved, on one hand, through an increase in Q (and therefore Q_m), making the
 639 flow approach the hydraulic limit (panel (b)), and on the other hand, through an
 640 increase in F , in particular through laminar interfacial shear (r_I), rendering the flow
 641 unstable to Holmboe waves above a certain threshold (L \rightarrow H transition, panel (c)).
 642 The phenomenology of this transition agrees with that proposed by the energetics
 643 of LPL19 (see their § 6.2-6.3). The fact that the L \rightarrow H (or L \rightarrow W) transition
 644 exhibits different scalings in our different data sets is not presently understood. It
 645 may come from the complex, individual roles of Q and F in the precise flow profiles
 646 $u(y, z), \rho(z)$ responsible for triggering the Holmboe instability, and the different
 647 scalings of Q and F that could allow $2QF$ to follow a θRe scaling.

648 (iii) At high θRe : the hydraulic limit is reached, the upper bound is tight ($b \approx 0$), the
 649 interface is mostly flat ($\eta(x) \approx 0$ everywhere), and the inequality (5.6) becomes
 650 $2QF \approx F \approx \theta Re$. In such *forced flows*, the friction parameter F alone must
 651 precisely balance the forcing. Arbitrarily large θRe requires arbitrarily large F ,
 652 which we conjecture is largely achieved by *turbulent interfacial* friction (increase in
 653 r_I responsible for the $H \rightarrow I$ and eventually the $I \rightarrow T$ transition).

654 From implication (iii), it is natural to conjecture that these two transitions are also caused
 655 by threshold values of the interfacial friction ratio r_I , which, as explain in appendix C.2,
 656 can be written $r_I = 1 + K_I$, where K_I is a turbulent momentum diffusivity (non-
 657 dimensionalised by the molecular value ν) parameterising interfacial Reynolds stresses
 658 (see (C 19)). Assuming that all wall shear stresses are similar ($r_Y \approx 1$), and that
 659 interfacial Reynolds stresses eventually dominate over laminar shear ($K_I \gg 1$), we have
 660 $K_I \approx F/(8f_Z)$. For $Re < 50A$, fully-developed boundary layers yield $f_Z \sim 1$, implying
 661 regime transitions scaling with (ignoring pre-factors)

$$K_I \sim \theta Re \quad \text{for } Re < 50A. \quad (5.7)$$

662 For $Re \gg 50A$, thin top and bottom wall boundary layer arguments similar to those of
 663 § 5.1 yield $f_Z \sim A^{1/2} Re^{-1/2}$, implying regime transitions scaling with

$$K_I \sim A^{1/2} \theta Re^{1/2} \quad \text{for } Re \gg 50A. \quad (5.8)$$

664 Comparing (5.7)-(5.8) to (5.1)-(5.2) we see that the $Re < 50A$ scaling obtained
 665 with frictional hydraulics is identical to that obtained by the energetics. However, the
 666 $Re \gg 50A$ scaling is different, and unfortunately it does not allow us to explain the
 667 regime transitions data (a $\theta Re^{1/2}$ or $\theta^2 Re$ scaling is never observed). In addition, direct
 668 estimations of friction coefficients using three-dimensional, three-component velocity
 669 measurements in all flow regimes (L18, § 5.5) suggest *a posteriori* that the assumption
 670 that $K_I \gg 1$ might only hold *beyond* the $I \rightarrow T$ transition, undermining its usefulness to
 671 predict the $H \rightarrow I$ and $I \rightarrow T$ transitions.

672 From implication (ii), we understand why the volume flux Q , and hence the mass flux
 673 Q_m , both increase with θ and Re in the L and H regimes, as observed in § 4.3. However
 674 lazy flows are under-specified; only one equation governs both the volume flux and friction
 675 ($2QF \sim \theta Re$), which does not allow us to obtain the value of the exponent γ in the scaling
 676 $Q \sim \theta Re^\gamma$. From implication (iii), we conjecture two potential reasons for the decrease of
 677 the mass flux Q_m in the T regime (labelled ‘a’ and ‘b’ in panels *b, c*). In scenario ‘a’, Q_m
 678 decreases due to increasing mixing despite the volume flux Q staying relatively constant
 679 ($2QF \sim F \sim \theta Re$). In scenario ‘b’, Q_m decreases partly due to mixing, and partly due
 680 to a decrease in Q (compensated by F increasing faster than θRe). Accurate Q and Q_m
 681 data obtained by volumetric measurements of velocity and density in L18 (figure 5.12(*b*))
 682 support scenario ‘b’ up to $\theta Re = 132$, but additional data are required to draw general
 683 conclusions.

684 The above frictional hydraulic model assumes a two-layer flow without any form of
 685 mixing, and thus ignores the behaviour of the interfacial thickness δ , which is the subject
 686 of the next section.

687 5.3. Mixing models

688 The importance and difficulty of modelling interfacial mixing in exchange flows has long
 689 been recognised (Helfrich 1995; Winters & Seim 2000). However, despite the existence of
 690 hydraulic models for multi-layered or continuously-stratified flows (Engqvist 1996; Lane-
 691 Serff *et al.* 2000; Hogg & Killworth 2004), to date there exists no ‘three-layer’ hydraulic

692 model allowing for the exchange of momentum or mass between the two counter-flowing
 693 layers suitable to our problem (which would violate most hydraulic assumptions). Below
 694 we review some experimental, numerical, and theoretical work most relevant to the scaling
 695 of Q_m , δ , and their relation to fundamental stratified turbulence properties such as
 696 diapycnal diffusivity and mixing efficiency.

697 5.3.1. *Turbulent diffusion models*

Cormack *et al.* (1974a) tackled natural convection in a shallow ($A \gg 1$) cavity with differentially heated walls. This problem is analogous to SID flows in the limit of maximum ‘interfacial’ thickness ($\delta = 1$) in which turbulent mixing dominates to such an extent that the exchange flow is only weakly stratified in the vertical (i.e. $\langle |\partial_z \rho| \rangle_z < 1$ because $|\rho(z = \pm 1)| < 1$) and becomes stratified in the horizontal (i.e. $|\partial_x \rho(z = \pm 1)| > 0$ and mean isopycnals are no longer horizontal). In their model, the horizontal hydrostatic pressure gradient is balanced only by a uniform vertical turbulent diffusion with constant K_T . Using the terminology of § 2.3, this balance could be called the hydrostatic-mixing (or ‘HM’) balance where ‘mixing’ plays a similar role to ‘viscosity’ in the ‘HV’ balance of § 2.3. Cormack *et al.* (1974a) solved this problem analytically and found:

$$Q = \frac{5}{384}(AK_T)^{-1}, \quad (5.9a)$$

$$Q_m = 4AK_T + \frac{31}{1451520}(AK_T)^{-3}, \quad (5.9b)$$

698 where we assumed a turbulent Prandtl number of unity for simplicity (i.e. the density
 699 equation has the same turbulent diffusivity). The above equations are adapted from
 700 equations (19) and (20) of Hogg *et al.* (2001) (in their review of the results of Cormack
 701 *et al.* (1974a)) to match our slightly different definitions of Q , Q_m , A and especially
 702 our definition of K_T as being non-dimensionalised by the inertial scaling $\sqrt{g'H}H/2$
 703 (giving $K_T = (4Gr_T)^{-1/2}$ where Gr_T is their ‘turbulent Grashof number’). We also
 704 contrast the the uniform diffusivity K_T in this model and the interfacial diffusivity K_I
 705 in the frictional hydraulics model of § 5.2.3, which have different roles and different
 706 non-dimensionalisation ($\sqrt{g'H}H/2$ vs ν , hence ‘ $K_T = K_I/Re$ ’). The predictions (5.9)
 707 were verified numerically and experimentally in two papers of the same series (Cormack
 708 *et al.* 1974b; Imberger 1974), but only hold in the ‘high-mixing’ limit of $AK_T > 1/15$
 709 below which inertia becomes noticeable and the assumptions start to break down (at
 710 $AK_T < 1/25$, Q and Q_m even exceed the hydraulic limit).

711 Hogg *et al.* (2001) built on the above results and developed a model with linear velocity
 712 and density profiles within an interfacial layer of thickness $\delta < 1$ and a uniform turbulent
 713 momentum and density diffusivity K_T . This models the ‘IHM’ balance, i.e. the transition
 714 between the Cormack *et al.* (1974a) $AK_T > 1/15$ high-mixing limit (the ‘HM’ balance
 715 where turbulent diffusion dominates over inertia, $\delta = 1$, and (5.9) holds) and the $AK_T \rightarrow$
 716 0 hydraulic limit (the ‘IH’ balance where inertia dominates over mixing, $\delta = 0$, and
 717 $Q = Q_m = 1/2$ holds). Hogg *et al.* (2001) argued that δ would increase diffusively during
 718 the ‘duct transit’ advective timescale A , and integrated the linear velocity and density
 719 profiles across the interfacial layer to find

$$\delta \approx 5(AK_T)^{1/2}, \quad (5.10a)$$

$$Q \approx \frac{1}{2} - \frac{5}{4}(AK_T)^{1/2}, \quad (5.10b)$$

$$Q_m \approx \frac{1}{2} - \frac{5}{3}(AK_T)^{1/2}, \quad (5.10c)$$

720 where the prefactors $5, 5^{5/4}, 5^{5/3}$ come from the imposed matching with the high-mixing
 721 solution (5.9). Hogg *et al.* (2001) validated these predictions with large eddy simulations
 722 and found good quantitative agreement for Q, Q_m, δ across the range $AK_T \in [1/2000, 1/15]$,
 723 below which convergence to the inviscid hydraulic limit was confirmed.

724 In order to use these models to explain the scaling of Q_m and δ with A, B, θ, Re, Pr ,
 725 we need to (i) extend them to the more complex ‘IHGM’ balance of SID flows in the I
 726 and T regimes in which gravitational forcing is present ($\theta > 0$); (ii) have a model for
 727 the scaling of K_T on input parameters (the above models prescribed K_T as an input
 728 parameter, but it is *a priori* unknown in the SID). To do so, we propose to use insight
 729 gained by the energetics and frictional hydraulics models.

730 First, following the results of LPL19 and § 5.1 on the average rate of turbulent
 731 dissipation, it is tempting to model K_T using a turbulence closure scheme like the mixing
 732 length or $K - \epsilon$ model, yet these require either a length scale or the turbulent kinetic
 733 energy, which are both unknown (only the *rate* of dissipation is known, see (5.1)-(5.2)).

Second, borrowing from the frictional hydraulics results of § 5.2, it seems natural to
 conjecture that the ‘Reynolds stresses’ interfacial diffusivity K_I in the I and T regimes
 may play a similar role to the uniform turbulent diffusivity in the present model. Recalling
 that by definition $K_T = K_I/Re$, combining the scalings (5.7)-(5.8) with (5.10) would
 suggest:

$$\delta \sim \frac{1}{2} - Q_m \sim (A\theta)^{1/2} \quad \text{for } Re < 50A, \quad (5.11a)$$

$$\delta \sim \frac{1}{2} - Q_m \sim (A^3\theta^2 Re^{-1})^{1/4} \quad \text{for } Re \gg 50A. \quad (5.11b)$$

734 Unfortunately these scalings are not consistent with the observations of figures 5-8: δ is
 735 clearly a function of Re for $Re < 50A$ (less so at high Re where the $A\theta$ scaling has indeed
 736 been observed by K91), and δ is clearly not a decreasing function of Re for $Re \gg 50A$.

737 5.3.2. Previous mixing efficiency measurements and models

738 In this section we discuss two studies of the interfacial layer thickness δ and its relation
 739 to the Richardson number and mixing efficiency as a basis for the development of a more
 740 suitable model for SID flows in the next section.

741 Prastowo *et al.* (2008) studied exchange flows through short ($A \approx 2-3$), wide ($B \gg 1$),
 742 horizontal ($\theta = 0$) contractions. Their measurements suggest an approximately constant
 743 interfacial thickness $\delta \approx 0.23 - 0.25$ across the range $Re \in [10^4, 10^5]$, in rough agreement
 744 with previously quoted estimates for shear-driven mixing flows (e.g. Sherman *et al.*
 745 (1978), p. 275 and references therein). They support this observation with ‘equilibrium’ or
 746 ‘marginally stable’ Richardson number arguments that the gradient Richardson number
 747 should be maintained near the Miles-Howard linear stability threshold, a phenomenon
 748 commonly observed subsequently in the observational literature on shear-driven mixing
 749 (Thorpe & Liu 2009; Smyth & Moum 2013). Assuming a linear profile for $u(z)$ and $\rho(z)$
 750 across the mixing layer yields $Ri_g \approx \delta \approx 0.25$.

751 Prastowo *et al.* (2008) also measured the time-averaged mixing efficiency in their
 752 exchange flow using density profile measurements in the reservoirs at the end of the
 753 experiments, defined as $\mathcal{M} \equiv (P_f - P_r)/(P_i - P_r) \in [0, 1]$, where P_i is the initial potential
 754 energy in the system (before the exchange flow starts), P_f is the final measured potential
 755 energy in the system, and P_r is the ‘reference’ or ‘minimum’ potential energy obtained
 756 by adiabatic (‘no-mixing’) rearrangement of fluid parcels from the initial conditions (i.e.
 757 $P_i - P_r$ is the initially available potential energy). They found collapse of the \mathcal{M} data with
 758 ARe and $\mathcal{M} \rightarrow 0.11$ for $ARe \rightarrow 10^5$ (using our notation). Finally, they supported this

observation and linked \mathcal{M} to δ by estimating mixing efficiency as the ratio of potential energy gain to kinetic energy deficit caused by the presence of a linear mixing layer, which yielded $\mathcal{M} \approx Ri_g/2 \approx \delta/2 \approx 0.125$.

Hughes & Linden (2016) studied horizontal lock exchange gravity currents, which behave similarly to our exchange flows for part of their life cycle. They measured $\delta \approx 0.33$ in the range $Re \in [10^4, 10^5]$. Using similar measurements to Prastowo *et al.* (2008), they found $\mathcal{M} \rightarrow 0.08$ asymptoting from below as $Re \rightarrow 10^5$. They supported this asymptotic value using a simple mixing model based on idealised linear profiles in the mixing layer, which yielded $\mathcal{M} = (2\delta^2/3)(1 - 2\delta/3)(1 - \delta/2)^{-2} \approx \delta^2 \approx 0.08$.

However, we have seen that exchange flows in inclined ducts have δ monotonically increasing not only with A and Re , but also with θ . In addition, much higher values of $\delta \gg 0.3$ (up to 0.8, and even 1 in K91) can be achieved even at moderate values of θ of a few α and $Re < 10^4$. Therefore, the above models supporting values of $\delta = 0.2 - 0.3$ and $\mathcal{M} = 0.08 - 0.12$ in the T regime disagree with our data, despite (i) the similarity of SID flows to the flows assumed above (shear-driven mixing flows with the same ‘IH’ velocity scaling $-1 \lesssim u \lesssim 1$) and (ii) the fact that these models would apparently not be modified by the presence of gravitational forcing ($\theta > 0$).

5.3.3. New mixing efficiency model

To address this, we propose a different model of mixing based on the energetics framework of LPL19. As sketched in figure 11(a), we consider that the duct is composed of three volume-averaged energy reservoirs (in bold): potential energy P , kinetic energy K , and internal energy I (heat). We further decompose the potential energy reservoir into an available potential energy P_A , and a background potential energy P_B (such that $P = P_A + P_B$), as is customary in the study of mixing (see e.g. Winters *et al.* (1995)).

As explained in LPL19 (see their § 4.1-4.3 and figure 8(b)), forced flows have, to a good approximation, the following quasi-steady-state energetics: the external fluid reservoirs provide an advective flux of potential energy into the duct, which we identify here as being an advective flux of *available* potential energy $\Phi_{P_A}^{\text{adv}} \approx Q_m \theta / 8$, which is then converted to kinetic energy by the horizontal buoyancy flux B_x , and to heat by the viscous dissipation $D \approx (2/Re) \langle s^2 \rangle_{x,y,z,t}$. When turbulent mixing is neglected, all these fluxes have equal magnitude, and $D \approx (1/8)Q_m \theta$. When turbulent mixing is included, a net vertical buoyancy flux B_z converts part of K back to P_A , and a net irreversible diapycnal flux Φ^d converts part of P_A to P_B , at a steady-state rate equal to the advective flux of P_B out of the duct, back into the external reservoirs $|\Phi_{P_B}^{\text{adv}}| = |\Phi^d|$. The mixing efficiency quantifies the percentage of total time- and volume-averaged power throughput $\Phi_{P_A}^{\text{adv}}$ that is spent to irreversibly mix the density field inside the duct:

$$\mathcal{M} = \frac{\Phi^d}{D + \Phi^d} = \frac{\Phi_{P_B}^{\text{adv}}}{\Phi_{P_A}^{\text{adv}}}. \quad (5.12)$$

It is expected that $\mathcal{M} \ll 1$ in such flows, as represented by the respective thickness of the arrows in figure 11(a), representing the order of magnitude of the fluxes.

As sketched in figure 11(b), we propose piecewise-linear flow profiles $u(z) = \rho(z)$ at either end of the duct as a minimal model to estimate the magnitude of $\Phi_{P_B}^{\text{adv}}$ as a function of the interfacial layer thickness δ , and eventually link it to input parameters A, θ, Re . We consider that fluid comes from the external reservoirs into the duct *unmixed* below (resp. above) the interfacial mixing layer at the left (resp. right) end of the duct, and leaves the duct *mixed* with a linear profile, going from 0 at the bottom (resp. top) edge of the mixed layer to -1 (resp. 1) at the top (resp. bottom) edge of the mixed layer. (In

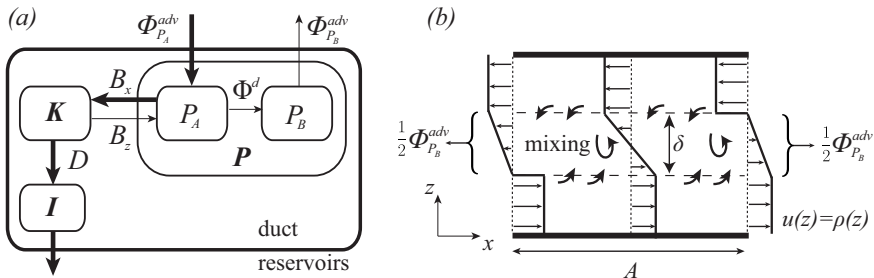


Figure 11: Mixing model for SID flows: (a) Time- and volume-averaged energetics model developing on that in LPL19 (their figure 8(b)) by subdividing the potential energy reservoir as $P = P_A + P_B$. We also show the kinetic energy K , internal energy I , and all relevant fluxes: horizontal buoyancy flux B_x , vertical buoyancy flux B_z , viscous dissipation D , diapycnal flux Φ^d and advective fluxes with the external reservoirs $\Phi_{P_A}^{adv}$, $\Phi_{P_B}^{adv}$. The direction of the arrows denotes the net (time-averaged) transfer, and the thickness of the arrows denotes the expected magnitude of the fluxes (with the expectation that $\Phi_{P_A}^{adv} \approx B_x \approx D$ and $B_z \approx \Phi^d \approx \Phi_{P_B}^{adv}$). (b) Simplified flow model in the duct to estimate the mixing rate from $\Phi_{P_B}^{adv}$ and link it to δ . The in-flow of unmixed fluids from the external reservoirs and the out-flow of mixed fluid back into them are modelled by the broken line profiles $u(z) = \rho(z)$ drawn at the left and right ends of the duct (consistent with the typical mid-duct profile drawn, equal to $u = \rho = \pm 1$ above and below the mixing layer and $u = \rho = -2z/\delta$ in the mixing layer, assumed elsewhere in the literature).

804 more central sections of the duct, mixing smoothes out the discontinuities at the edges of
 805 the mixing layer present at the ends, and we expect the continuous linear profile drawn
 806 in the centre, but it is irrelevant to the following calculations.) The outflow of mixed fluid
 807 creates the following net flux of background potential energy out of the duct:

$$\Phi_{P_B}^{adv} = \frac{1}{4A} \langle z\rho u \rangle_z |_{L-R} = \frac{2}{4A\delta} \int_{-\delta/2}^{\delta/2} z \left(z + \frac{\delta}{2} \right)^2 dz = \frac{\delta^3}{24A}, \quad (5.13)$$

808 where $|_{L-R}$ denotes the difference between the values at the left and right boundary,
 809 and the prefactor $1/(4A)$ comes from the non-dimensionalisation of the energy budget
 810 equations (see LPL19, equation (4.14a)). From (5.12)-(5.13) and $\Phi_{P_A}^{adv} \approx Q_m \theta / 8$, we now
 811 deduce:

$$\delta \approx (3A\theta Q_m \mathcal{M})^{1/3}. \quad (5.14)$$

812 Encouragingly, this estimation has the potential to be consistent with our data in the
 813 SID. Assuming that $Q_m \approx 0.5$ throughout most of the I and T regimes, we conjecture
 814 that most of the dependence on Re observed in the δ data of figure 7 is due to the
 815 underlying monotonic increase of $\mathcal{M}(Re)$, which is *a priori* unknown, but consistent with
 816 the observations of Prastowo *et al.* (2008) and Hughes & Linden (2016). The observation
 817 of K91 and figure 7(a-b) that δ primarily scales with the group $A\theta$ at $Re \gg 500A$ (as
 818 sketched in figure 3(c)) would suggest that \mathcal{M} asymptotes to a constant value at high
 819 Re , which is also consistent with the observations of Prastowo *et al.* (2008) and Hughes
 820 & Linden (2016) at $ARe > 10^5$ and $Re > 10^5$ respectively. Assuming their high- Re
 821 asymptotic value of $\mathcal{M} \approx 0.1$, we obtain

$$\delta \rightarrow 0.5 \left(\frac{\theta}{\alpha} \right)^{1/3}. \quad (5.15)$$

822 This gives, for example, $\delta \approx 0.4$ when $\theta/\alpha \approx 1/2$. This value agrees with the K91 data
 823 (figure A.1(*f-g*)) and our LSID data (figure 7(*a*), at $Re > 10^4$ and $ARe > 10^5$). However,
 824 this value does not agree well with our HSID, tSID, and mSID δ data (figure 7(*b-d*)),
 825 in which δ remains dependent on Re . This is presumably due to the lower values of A
 826 and/or Re in these data sets, which remain below the asymptotic values of $Re > 10^5$
 827 and $ARe > 10^5$. In other words, we believe that our δ data and (5.15) are consistent and
 828 provide further (albeit indirect) evidence for the monotonic increase of \mathcal{M} with Re .

829 6. Conclusions

830 6.1. Problem and approach

831 In this paper, we investigated buoyancy-driven exchange flows taking place in inclined
 832 rectangular ducts (figure 1). We focused on the behaviour of three key dependent
 833 variables: the qualitative flow regime (laminar, wavy, intermittently turbulent, or fully
 834 turbulent), the non-dimensional mass (or buoyancy) flux Q_m , and the non-dimensional
 835 thickness of the interfacial layer δ as the five non-dimensional input parameters were
 836 varied: the duct longitudinal aspect ratio A , spanwise aspect ratio B , tilt angle θ ,
 837 Reynolds number Re , and Prandtl number Pr .

838 Dimensional analysis (figure 2) and the experimental literature (figure 3, appendix A
 839 and table A.1) showed that the rich dynamics of these sustained stratified shear flows
 840 were accessible for a wide range of Re and for θ of at most a few duct aspect ratios
 841 $\alpha = \tan^{-1}(A^{-1})$. Our focus on ‘long’ ducts ($A \gg 1$) allowed us to explore these dynamics
 842 while keeping $\theta = O(\alpha)$ small enough to remain relevant to largely-horizontal, stably-
 843 stratified geophysical flows and turbulence, which are our ultimate motivation.

844 To overcome the limitations of previous studies of the problem, we presented extensive
 845 experimental results for all three variables of interests (regimes, Q_m , and δ) in the (θ, Re)
 846 plane for five different data sets, between which A, B, Pr were varied systematically
 847 (table 1).

848 6.2. Experimental results

849 First, our data (figures 4-8) confirmed the conclusions of past studies: that increasingly
 850 disordered and turbulent regimes are found as A, θ, Re are increased, that Q_m is non-
 851 monotonic in θ and Re , and that δ is monotonic in A, θ, Re . Second, our data revealed
 852 the existence and importance of at least one additional non-dimensional input parameter
 853 involving the dimensional height of the duct H and a ‘missing’ length scale, because our
 854 regime, Q_m , and δ data at the same A, B, θ, Re, Pr but different H do not collapse. This
 855 missing length scale has been an enduring puzzle that remains unsolved. Third, our data
 856 highlighted the complex dependence of all variables on all five parameters A, B, θ, Re, Pr .
 857 Regime transition, iso- Q_m , and iso- δ curves are not only shifted in the (θ, Re) plane at
 858 different A, B , or Pr , but they also generally exhibit different power law scalings in θ
 859 and Re at different A, B, Pr .

860 Given the breadth of our observations summarised above, and the relative richness of
 861 our data in the (θ, Re) plane compared to the few values of A, B, Pr studied, we focused
 862 specifically on the very last observation above, i.e. on the various scalings of the form
 863 $\theta Re^\gamma = \text{const.}$ governing the regime transitions curves and the major axis of hyperbolas
 864 best fitting Q_m in the $(\log \theta, \log Re)$ plane. Even within this specific focus, we discovered
 865 that γ not only varies between data sets (at different A, B, Pr) but that it also varies
 866 within a given data set (at fixed A, B, Pr): (*i*) γ is generally different for the regime data
 867 ($\gamma = 1$ or 2) and the Q_m data ($0.3 < \gamma < 2.6$) implying that regime and Q_m are not well

868 correlated (whereas regimes and δ are); and (ii) in one regime data set, γ even takes two
 869 different values (of 1 and 2) in different regions of the (θ, Re) plane.

870 6.3. Modelling results and outlook

871 To provide a modelling framework to understand the above observations (i)-(ii), we
 872 first split the (θ, Re) plane into four quadrants delimited by $\theta = \alpha$ (the ‘lazy/forced’ flow
 873 boundary, based on the respective dominance of hydrostatic/gravitational forcing) and
 874 $Re = 50A$ (the ‘low/high Re ’ boundary, based on whether or not boundary layers are
 875 fully developed across the duct). We then discussed three families of candidate models.

876 In § 5.1 we considered the volume-averaged energetics framework of Lefauve *et al.*
 877 (2019) (LPL19). LPL19 physically explained the $\theta Re = \text{const.}$ scaling of regime transi-
 878 tions of forced ($\theta \gtrsim \alpha$), low- Re ($Re \lesssim 50A$), salt-stratified ($Pr = 700$) flows as being
 879 caused by threshold values of the three-dimensional kinetic energy dissipation (equation
 880 (5.1)). We carried out the natural extension of their argument to high- Re ($Re \gg 50A$)
 881 flows, by accounting for two-dimensional, laminar boundary layer dissipation. However,
 882 the resulting predicted scaling in $\theta Re - A^{-1/2} Re^{1/2}$ (equation (5.2)) did not agree with
 883 any of our regime data. Detailed measurements of dissipation in these high- Re flows (not
 884 found in LPL19) would be valuable to understand why this is the case, but they are very
 885 challenging to perform due to the required spatio-temporal resolution.

886 In § 5.2 we developed a two-layer frictional hydraulics model of SID flows (figure 9)
 887 from Gu & Lawrence (2005) and showed that the existence of a solution imposed a lower
 888 and upper bound on the product of the volume flux by a parameter quantifying wall and
 889 interfacial friction (equation (5.6)). This model explained the qualitative behaviour of
 890 Q_m with θRe , and the fact that regimes and Q_m could have different scalings (figure 10).
 891 This model also provided a quantitative scaling for the interfacial friction parameter
 892 and, in turn, for regime transitions, based on our conjecture that regime transitions were
 893 directly linked to interfacial turbulent stresses. Although the resulting low- Re scaling in
 894 θRe (equation (5.7)) was identical to that predicted by the energetics model and correct
 895 (at least for $Pr = 700$), the high- Re scaling in $A^{1/2} \theta Re^{1/2}$ (equation (5.8)) did not agree
 896 with our regime data.

897 Neither the energetics nor the frictional hydraulics model could predict the observed
 898 scalings in θRe or θRe^2 observed in lazy flows ($\theta \lesssim \alpha$) because these flows are under-
 899 specified in either model (they have more unknowns than equations). In addition, scalings
 900 laws deduced from plots in the $(\log \theta, \log Re)$ plane break down for lazy flows at slightly
 901 negative angles ($-\alpha \lesssim \theta \lesssim 0$), which we largely ignored in this paper.

902 In § 5.3, we focused on the scaling of δ underpinned by turbulent mixing. We first
 903 considered a model with constant turbulent diffusivity imposed throughout the domain
 904 (Cormack *et al.* 1974a; Hogg *et al.* 2001). We attempted to link this diffusivity to input
 905 parameters following insights gained from frictional hydraulic theory, but the resulting
 906 scalings (equation (5.11)) did not agree with our data. We then explained why previous
 907 measurements and models of δ in related stratified shear flows (Prastowo *et al.* 2008;
 908 Hughes & Linden 2016) were inconsistent with our results on exchange flows in inclined
 909 ducts. We thus developed a new model that explicitly represents the rate of mixing in
 910 the energy budget analysis of LPL19, and quantifies this mixing as a function of known
 911 input parameters and an unknown mixing efficiency \mathcal{M} using a simplified flow profile
 912 (figure 11, equation (5.13)). The resulting expression for δ (equations (5.14)-(5.15)) is
 913 qualitatively consistent with our observations, but it involves \mathcal{M} (not measured in these
 914 experiments) whose scaling on Re is critical. Our model and data indirectly support
 915 previous observations of Prastowo *et al.* (2008) and Hughes & Linden (2016) that \mathcal{M}

916 monotonically increases with Re to reach asymptotic values of $\mathcal{M} \approx 0.1$ at very high Re ,
 917 but direct measurements of \mathcal{M} are needed to confirm this.

918 While these models have allowed us to make significant progress by providing useful
 919 physical insights and partial quantitative results regarding scaling laws in A, θ, Re , our
 920 experimental observations have raised an even larger number of questions which remain
 921 open. Among these are the elusive existence of an sixth non-dimensional input parameter,
 922 the influence of the spanwise aspect ratio B and Prandtl number Pr , and the scaling of
 923 the mixing efficiency \mathcal{M} .

924 Acknowledgements

925 AL was supported by an Engineering and Physical Sciences Research Council (EPSRC)
 926 Doctoral Prize Fellowship. We also acknowledge funding from EPSRC under the Pro-
 927 gramme Grant EP/K034529/1 ‘Mathematical Underpinnings of Stratified Turbulence’
 928 (MUST) and from the European Research Council (ERC) under the European Union’s
 929 Horizon 2020 research and innovation Grant No 742480 ‘Stratified Turbulence And
 930 Mixing Processes’ (STAMP). We thank Colin Meyer and Simon Vincent for collecting the
 931 regime and mass flux data in the LSID and HSID geometries in 2012-2014, and we thank
 932 Ling Qu visiting from the South China Sea Institute of Oceanology (SCSIO, Guangzhou,
 933 China) for collecting part of the regime and mass flux data in the mSID and tSID in 2015-
 934 2016. We also thank Darwin Kiel from Coanda Research & Development Corporation
 935 (Burnaby, Canada) for his reading of the manuscript, his suggestions, and his permission
 936 to reproduce some of his results. Finally, we are grateful for the invaluable experimental
 937 support and expertise of Stuart Dalziel, Jamie Partridge and the technicians of the G.
 938 K. Batchelor Laboratory. The data associated with this paper can be downloaded from
 939 the repository doi.org/10.17863/CAM.48821.

940 Declaration of Interests

941 The authors report no conflict of interest.

942 Appendix A. Literature review

943 In this section we support and complement the conclusions of § 3 by reviewing the
 944 experimental literature on the questions of flow regimes (§ A.1), mass flux (§ A.2), and
 945 interfacial layer thickness (§ A.3). We limit the discussion to the results that are most
 946 relevant to this paper, and give further details about the geometry and parameters used
 947 in each study in table A.1.

948 A.1. Flow regimes

949 Macagno & Rouse (1961) (MR61) constitutes, to our knowledge, the first experimental
 950 study in a setup similar to the SID. MR61 used dye visualisations to describe four
 951 qualitatively different regimes:

952 L ‘uniform laminar motion with straight streamlines’;

953 W ‘laminar motion with regular waves’;

954 I ‘incipient turbulence, with waves which break and start to show irregularity and
 955 randomness’;

956 T ‘pronounced turbulence and active mixing across the interface’

957 MR61 mapped the above regimes together with measurements of the interfacial stress

and mixing coefficients in the plane (F_*, R_*) , where $F_* \approx 2\sqrt{2}Q$ and $R_* \approx 4QRe$ (using our notation) are ‘effective’ Froude and Reynolds numbers. Arguing that flows above a certain R_* and F_* would be unstable, they proposed and verified experimentally that the ‘transition curves’ separating the flow regimes and the iso-curves of interfacial shear and mixing coefficients scaled with $R_* F_* \approx Re Q^2$ (i.e. these curves are $Re Q^2 = \text{const.}$). As we have seen in § 2.3, Q is in reality a dependent variable, not an input parameter. This confusion in MR61 comes from the fact that their setup (which they attribute to Helmholtz) differs from the SID in that they were able to prescribe the volume flux Q by controlling the inflow of salt water by a piston communicating with one of the reservoirs (their system was closed, i.e. it had no free surface). They varied Q, θ to reach target values of R_*, F_* , without apparently realising that the flow was hydraulically controlled and that θ and Re were the relevant independent input parameters.

Wilkinson (1986) (W86) used shadowgraph and observed regime transitions similar to MR61 in a horizontal, circular pipe: ‘shear-induced instabilities [...] initially in the form of cusp-like waves, but as the shear was further increased, Kelvin-Helmholtz billows were seen to grow and collapse creating a turbulent shear layer’. He suggested a scaling in Re alone, independent of A : laminar flow under $Re < 2450$, ‘interfacial waves radiating in both directions’ for $Re \in [2600, 2700]$, and turbulence for $Re > 2700$, but his experiments were limited in number (≈ 18).

Kiel (1991) (K91) used shadowgraph and laser sheet visualisations at larger Re , and classified the regimes differently: laminar; turbulent with $\delta < 1$; and turbulent with $\delta = 1$. Using a semi-empirical model based on the ratio of ‘IG’ to ‘IH’ kinetic energy scales (see § 2.3), he proposed regime transitions scaling with a ‘geometric Richardson number’ $Ri_G \sim A \tan \theta$ (more details in § A.2) independently of Re , i.e. the opposite of W86.

Meyer & Linden (2014) (ML14) used shadowgraph visualisations, and (unaware of MR61) described essentially the same four regimes of MR61:

- L laminar flow with a thin, flat density interface;
- H mostly laminar flow with quasi-periodic waves on the density interface, identified as Holmboe waves;
- I spatio-temporally intermittent turbulence with small-scale structures and noticeable mixing between the two layers;
- T statistically-steady turbulent flow with a thick interfacial density layer.

Interestingly, the only difference between the MR61 and ML14 nomenclatures lies in the letter characterising the wavy regime (W in MR61 and H in ML14), simply because MR61 observed Holmboe waves (see their figure 5) before they were explained by Holmboe (1962). ML14 mapped these regimes in the (θ, Re) plane for two different $A = 15, 30$. They argued that, because the flow was hydraulically controlled, the ‘excess kinetic energy’ gained by the flow at $\theta > 0$ (i.e. the square of the ‘IG’ velocity scaling $g'L \sin \theta$) should be dissipated turbulently. By non-dimensionalising this excess energy by $(\nu/H)^2$, ML14 proposed and verified that regime transitions scale with a Grashof number (see their equation 4.4)

$$Gr \equiv \frac{g'L \sin \theta}{(\nu/H)^2} \approx 4A\theta Re^2, \quad (\text{A1})$$

This scaling has two limitations: the ‘IG’ energy does not explain the transitions at $\theta = 0$, and its non-dimensionalisation by $(\nu/H)^2$ lacks a physical basis.

Lefaue *et al.* (2019) (LPL19) repeated the shadowgraph observations of ML14 in a smaller duct ($H = 45$ mm vs $H = 100$ mm) with otherwise equal parameters (A, B, Pr) =

1004 (30, 1, 700) and mapped the regimes in the (θ, Re) plane. LPL19 observed two distinct
 1005 scalings: a θRe^2 scaling for $\theta \lesssim \alpha$ (in agreement with ML14), and a θRe scaling for
 1006 $\theta \gtrsim \alpha$ (not observed in ML14). They developed from first principles energy budgets
 1007 which they applied to 16 experiments in which the full density field and three-component
 1008 velocity field were simultaneously measured in a three-dimensional volume of the duct
 1009 (for visualisations of flow fields in all four regimes, see their figures 2-3). They showed that
 1010 for $\theta \gtrsim \alpha$ (for so-called ‘forced flows’), the time- and volume-average rate of dissipation
 1011 of kinetic energy could be predicted *a priori* as

$$\langle \mathbf{s}_{ij} \mathbf{s}_{ij} \rangle_{x,y,z,t} \approx \frac{1}{16} \theta Re, \quad (\text{A } 2)$$

1012 where \mathbf{s} is the non-dimensional strain rate tensor. Because the magnitude of stream-
 1013 wise velocities and wall shear stresses are bounded to $O(1)$ by hydraulic control, the
 1014 requirement of high strain rates at high θRe caused transitions to increasingly three-
 1015 dimensional (turbulent) flow regimes with smaller-scale gradients. The θRe scaling of
 1016 energy dissipation matched the observed regime transitions in ‘forced flow’ ($\theta \gtrsim \alpha$), but
 1017 the θRe^2 transition scaling in ‘lazy flows’ ($\theta \lesssim \alpha$) remains unexplained.

1018 A.2. Mass flux

1019 Leach & Thompson (1975) (LT75) measured $Q_m = 0.23$ in horizontal circular pipes
 1020 for high Reynolds number $Re = O(10^4 - 10^5)$, and $Pr = 1$ and 700 (respectively CO_2/air
 1021 and salt/fresh water). Surprisingly, they observed no dependence on A, Re, Pr .

1022 Mercer & Thompson (1975) (MT75) reported dramatic non-monotonicity of $Q_m(A, \theta)$:
 1023 $Q_m \approx 0.2 - 0.3$ at $\theta = 0^\circ$ (in agreement with LT75), increasing to $Q_m \approx 0.4$ at $\theta \approx \alpha/2$,
 1024 and decreasing to $Q_m \approx 0.01 - 0.1$ at $\theta = 90^\circ$ (we reproduce some of their data in
 1025 figure A.1(b)). In a small set of experiments at $\theta = 30^\circ$ in a larger pipe ($Re = 2 \times 10^4$
 1026 vs 2×10^3 , and $A = 6$), they reported dependence on Re even in the ‘very high’ range
 1027 $Re \in [300A, 3000A]$ (though it might be due to subtle differences in apparatus).

1028 W86 developed a Bernoulli model in a horizontal circular pipe which predicted an
 1029 upper bound of $Q = \pi/8 \approx 0.39$ (non-dimensionalised using the pipe diameter), making
 1030 the analogy with the hydraulic control arguments in Wood (1970) who predicted $Q = 0.5$
 1031 in rectangular ducts. Including viscous boundary layers at the circular walls, he predicted
 1032 and verified experimentally a monotonic increase of Q with $A^{-1} Re$ (as the thickness of
 1033 boundary layers decreases): $Q_m = 0.13$ at $Re \approx 20A$ to $Q_m = 0.35$ at $Re \approx 500A$ (larger
 1034 than LT75), in agreement with the dimensional analysis of § 2.3 (conclusion (ii)).

1035 K91 developed an inviscid Bernoulli model in an inclined duct for two counter-flowing
 1036 layers of equal thickness and predicted $Q \approx \sqrt{(4/9) \cos \theta + A \sin \theta}$. In agreement with
 1037 our dimensional analysis in § 2.3, this expression predicts a transition from an ‘IH’
 1038 balance at $0 < \theta \ll \alpha$ with $Q \approx 2/3$ to an ‘IG’ balance at $\theta \gg \alpha$ with $Q \approx \sqrt{A \sin \theta}$.
 1039 K91 showed, however, that this ‘IG’ scaling could only be observed experimentally
 1040 when communication and mixing between the two counter-flowing layers was artificially
 1041 suppressed by a rigid ‘splitter plate’ along the duct. He argued that the non-realisation
 1042 of the IG scaling was due to a turbulent transition occurring when the IG scaling for Q
 1043 ‘that potentially exists’ exceeds a threshold dependent on the ‘stabilising effect of $g' \cos \theta$ ’,
 1044 leading to his definition of ‘geometric Richardson number’ whose inverse we interpret as
 1045 being the square ratio of the ‘potential’ (‘IG’) to the ‘maximal’ (‘IH’) volume flux Q :

$$Ri_G^{-1} \equiv \left(\frac{\sqrt{(4/9) \cos \theta + A \sin \theta}}{(1/2) \sqrt{\cos \theta}} \right)^2 = \frac{16}{9} + 4A \tan \theta = \frac{16}{9} + 4 \frac{\tan \theta}{\tan \alpha}. \quad (\text{A } 3)$$

1046 K91’s unpublished data in reproduced in figure A.1. K91 obtained good collapse of his

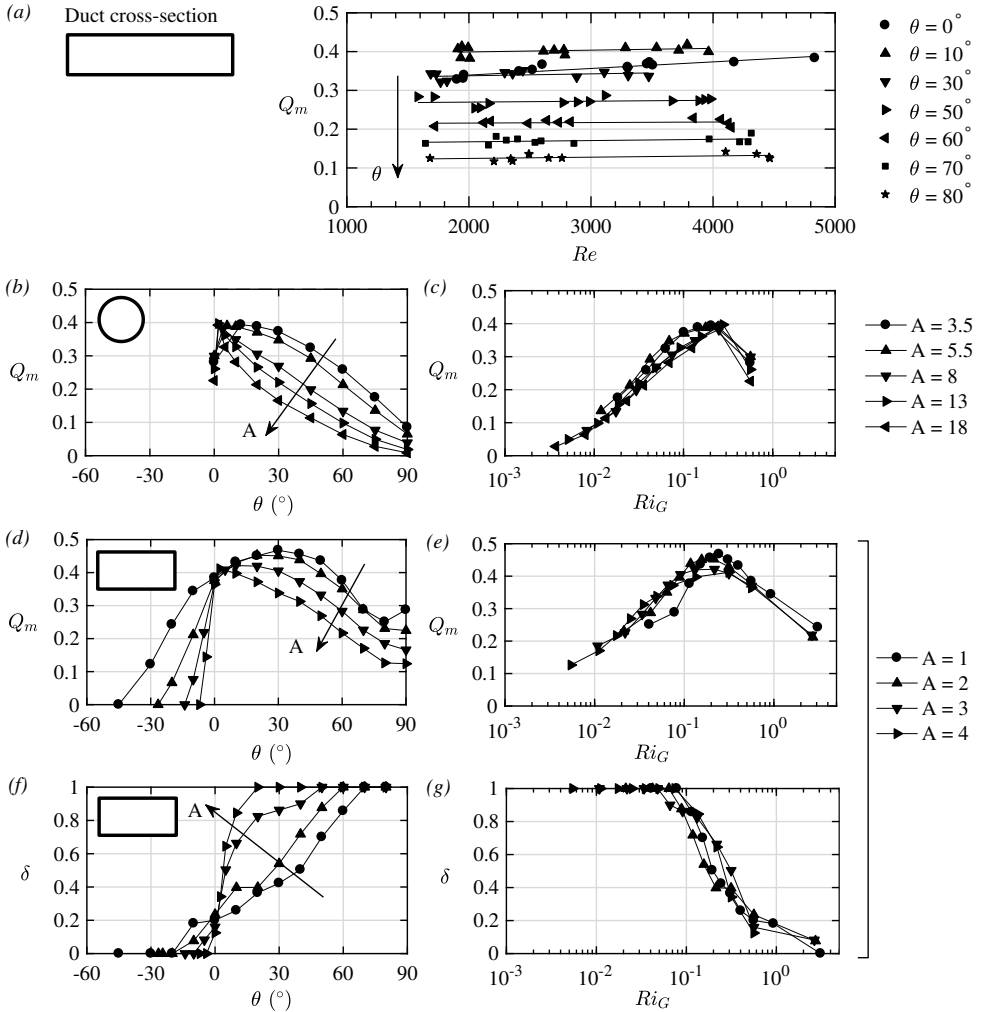


Figure A.1: Unpublished experimental data in Kiel (1991), reproduced with his permission. (a) Independence of Q_m on Re at $A = B = 4$. Left panels: (b) MT75's $Q_m(A, \theta)$ data in a circular pipe, (d) K91's $Q_m(A, \theta)$ data and (f) $\delta(A, \theta)$ data, both at $B = 2$. Right panels (c, e, g): collapse of the data in the respective left panel with Ri_G . These data have been converted to follow our notation and non-dimensionalisation.

1047 and MT75's Q_m data with $Ri_G \sim A \tan \theta$, with a peak at $\theta \approx \alpha/2$, and a decay at larger
 1048 θ for a range of A and θ (figure A.1b-e corresponding to his figures 2.6 and 5.2). Further,
 1049 in agreement with W86's arguments, K91 reported independence of his results with Re
 1050 above $Re > 400A$ (figure A.1a) and intentionally focused on these high Re throughout.

1051 ML14 observed monotonic increase of $Q_m(\theta)$ with $Q_m \approx 0.2 - 0.3$ at $\theta = 0^\circ$ and
 1052 $Q_m \approx 0.5$ at $\theta = \alpha/2$. They did not comment on the hint of non-monotonic behaviour
 1053 suggested by their data for $\theta \gtrsim 2\alpha$.

1054 LPL19 observed (in passing) non-monotonic behaviour of $Q_m(\theta, Re)$. Their data are
 1055 well fitted by a hyperbolic paraboloid in the $\log \theta - \log Re$ plane, where $Q_m = \text{const.}$
 1056 curves are hyperbolas, with $Q_m \approx 0.5$ along the major axis $\theta Re^{3/2} = 100$ (θ in radians),
 1057 and Q_m decays on either side of it.

A.3. Interfacial layer thickness

1058

1059

1060

1061

1062

1063

1064

1065

K91 performed conductivity probe measurements, observed monotonic increase of δ with both A and θ (figure A.1(*f*)), good collapse with $Ri_G \sim A \tan \theta$ (figure A.1(*g*)), and independence on Re (presumably because of his focus on $Re > 500A$). The interfacial mixing layer is turbulent and thick ($\delta \approx 0.4 - 0.7$) at $\theta \approx \alpha/2$ and fills the whole duct height ($\delta = 1$) at $\theta \gtrsim 2\alpha$. At even larger tilt angles, the mean vertical density gradient $|\rho(z = 1) - \rho(z = -1)|/2$ drops below 1 (this ‘extreme’ turbulent scenario falls outside the scope of this paper).

Table A.1: Synthesis of the literature review. For each paper, we specify the scale of the apparatus (duct height or pipe diameter H), the parameters that were either fixed or whose variation was not studied, those that were varied and studied, the key conclusions about the scaling of transitions between flow regimes (based on empirical or physical arguments), mass flux Q_m , and interfacial layer thickness δ .

| Name | H (mm) | Fixed params. | Varied params. | Regimes | Mass flux Q_m | Interfacial thickness δ |
|-------|----------------------|--|---|--|---|--|
| MR61 | 150 | $A = 6$ $B = 1/3$ $Re \approx 2 \times 10^3$ $Pr = 700$ | $\theta \in ?$ | $\sim Re Q^2$ (empirical) | — | — |
| LT75 | 150 – 1140 (pipe) | $B = 1$ $\theta = 0^\circ$ | $A \in [0.5, 20]$ $Re \in [15, 75] \times 10^3$ $Pr = 1, 700$ | — | Constant in A, Re, Pr at $\theta = 0^\circ$ $Q_m \approx 0.23$ | — |
| MT75 | 50, 150 (pipe) | $B = 1$ $Pr = 700$ | $A \in [0.5, 18]$ $Re = 2, 20 \times 10^3$ $\theta \in [0^\circ, 90^\circ]$ | — | Non-monotonic in A, θ $Q_m \approx 0.3$ at $\theta = 0^\circ$ $Q_m \approx 0.4$ at $\theta \approx \alpha/2$ $Q_m \rightarrow 0$ as $\theta \gg \alpha$ Dependence on Re | — |
| W86 | 14 – 25 (pipe) | $B = 1$ $\theta = 0^\circ$ $Pr = 700$ | $A = 1.6, 3.5, 9.6$ $Re \in [0.2, 3] \times 10^3$ | $\sim Re$ (empirical) | Monotonic in $A^{-1} Re$ $Q_m \approx 0.15$ at $Re \approx 20A$ $Q_m \approx 0.35$ at $Re \approx 500A$ | — |
| K91 | 50, 100 | $B = 1, 2, 4$ $Re \in [2, 15] \times 10^3$ $Pr = 700$ | $A = 1, 2, 4, 8$ $\theta \in [-45^\circ, 90^\circ]$ | $\sim A \tan \theta$ (empirical) | Non-monotonic in A, θ Collapse with $A \tan \theta$ Independence on Re | Monotonic in A, θ Max. $\delta = 1$ at $\theta \approx 2\alpha$ Collapse with $A \tan \theta$ |
| ML14 | 100 | $B = 1$ $Pr = 700$ | $A = 15, 30$ $\theta \in [-1^\circ, 4^\circ]$ $Re \in [1, 20] \times 10^3$ | $\sim A \theta Re^2$ (empirical) | Monotonic in θ $Q_m \rightarrow 0.5$ as $\theta > \alpha/2$ | — |
| LPL19 | 45 | $A = 30$ $B = 1$ $Pr = 700$ | $\theta \in [-1^\circ, 6^\circ]$ $Re \in [0.3, 6] \times 10^3$ | $\sim \theta Re^2$ as $\theta \lesssim \alpha$ (empirical) $\sim \theta Re$ as $\theta \gtrsim \alpha$ (physical) | Non-monotonic in θ, Re | — |

Appendix B. Experimental methodology

B.1. Flow regimes

Regimes were largely determined by shadowgraph observations over a subsection of the length of the duct, following the qualitative description of each regime of ML14 (see their § 3.1 and figure 3). For a schematic of the shadowgraph setup, see L18, § 2.1.

In the mSID data set, 48 out of 360 regime identifications were not made by shadowgraph, but rather by direct visualisation of the density field by planar laser induced fluorescence (PLIF), since more detailed measurements of the velocity and density fields (incompatible with simultaneous shadowgraph) have been performed in this geometry (Lefauve *et al.* 2018; Partridge *et al.* 2019; Lefauve *et al.* 2019).

All raw video data, including those obtained by other experimenters (acknowledged at the end of the paper), were reprocessed in an effort to ensure that regimes were identified as consistently as possible across all five data sets of table 1 (especially in the cases where the distinction between regimes can be subtle).

Most of the shadowgraph data (still images and movies) are available on the repository doi.org/10.17863/CAM.48821, and some of the velocity and density data are available on the repository doi.org/10.17863/CAM.41410 (linked to Lefauve *et al.* (2019)).

B.2. Mass flux

Mass fluxes were determined, as in ML14, by measuring the average initial ('i') and final ('f') density in each reservoir: reservoir '1', initially at density $\rho_1^i = \rho_0 + \Delta\rho/2$ and finally at a well mixed density ρ_1^f and '2', initially at $\rho_0 - \Delta\rho/2$ and finally at ρ_2^f , giving the following two estimations

$$\tilde{Q}_{m,1} = \frac{-(\rho_1^f - \rho_1^i)V_1}{\Delta\rho(H^2/2)\sqrt{g'H}T} \quad \text{and} \quad \tilde{Q}_{m,2} = \frac{(\rho_2^f - \rho_2^i)V_2}{\Delta\rho(H^2/2)\sqrt{g'H}T}, \quad (\text{B } 1)$$

where V_1, V_2 are the (typically approximately equal) volumes of fluid in the respective reservoirs, and the tilde on \tilde{Q}_m stresses the fact that they are non-dimensional (despite all quantities on the right side of the = sign being dimensional). Experiments in which both estimates differed by more than $(Q_{m,1} - Q_{m,2})/(Q_{m,1} + Q_{m,2}) > 10\%$ were rejected (typically due to an initial misadjustment of the free surfaces resulting in a net volume flux $\langle u \rangle_{x,y,z,t} \neq 0$). All data shown in this paper thus have near-zero net volume flux, and we only use the average value $Q_m \equiv (Q_{m,1} + Q_{m,2})/2$.

We recall that T in (B 1) is the (dimensional) duration of an experiment. The determination of the relevant T was made carefully but remains subject to intrinsic uncertainties which affect Q_m as we explain next. The duct is opened at time t^a initiating a gravity current lasting until the exchange flow is considered fully established by shadowgraph visualisations at time t^b . The exchange flow of interest continues until the levels of the discharged fluids approach the ends of the duct, at which point one end of the duct is closed at time t^c , shortly before the other end of the duct is closed at t^d . To avoid under- and over-estimations of Q_m by the intervals $t^d - t^a$ and $t^c - t^b$ (respectively), we choose to use the average of the two $T = (t^d - t^a + t^c - t^b)/2$, and to use error bars to indicate the magnitude of the resulting uncertainty (the difference between the over- and under-estimation). Note that error bars tend to be larger at high Re (figure 7) because the overall duration T of an experiment is inversely proportional to the magnitude of the dimensional exchange velocities (scaling with $\sqrt{g'H}$, and hence with Re) due to the finite size of the reservoirs. A smaller duration T increases the relative duration of initial transients (typically fixed) and therefore the uncertainty about T .

Note that measurements of Q_m in temperature-stratified experiments (mSIDT data

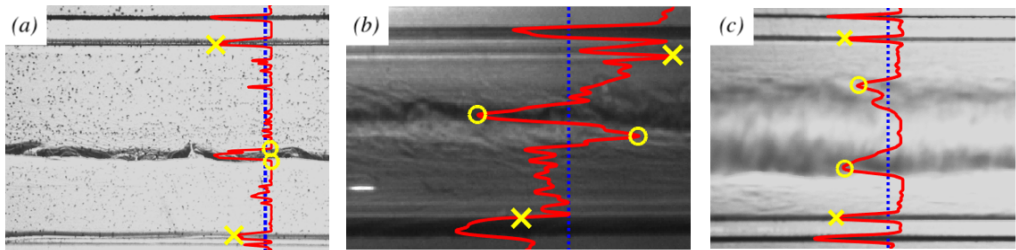


Figure B.1: Example of the determination of δ from shadowgraph snapshots in the (a) H regime (LSID) where $\delta = 0.069$; (b) I regime (mSID), where $\delta = 0.14$; (c) T regime (LSID), where $\delta = 0.47$. At a randomly chosen streamwise position (dotted blue line), the greyscale intensity $I(z)$ (solid red curve) is automatically overlaid using a convenient horizontal scale. The positions of the interfacial density layer and of the top and bottom walls are carefully clicked by hand (identified by the yellow circles and crosses respectively), and δ is determined as the ratio of the spacing between the pair of circles and crosses.

1112 set) could not be performed due to the practical impossibility to control the heat loss
 1113 occurring through the boundaries of the reservoir and the free surface.

1114 For more details on these measurements, see L18, § 2.2.

1115 All mass flux data (including $Q_{m,1}$ and $Q_{m,2}$, and for mSID and tSID the upper and
 1116 lower bound estimations using $T = t^d - t^a$ or $t^c - t^b$) are available on the repository
 1117 doi.org/10.17863/CAM.48821.

1118

B.3. Interfacial layer thickness

1119 The interfacial density layer thickness δ was estimated from shadowgraph images. To a
 1120 reasonable approximation, the refraction of near-parallel light beams by inhomogeneities
 1121 in the density field results in a recorded greyscale light intensity $I(x, z)$ proportional
 1122 to the second vertical derivative of the density field integrated in the spanwise direction
 1123 $I(x, z) \propto \int_{y=-B}^B \partial_{zz}^2 \rho dy$ (for a full derivation and discussion of the approximations, see
 1124 L18, § 2.1). This makes shadowgraphy particularly well-suited to detect the average
 1125 location of large-scale curvatures in the density field, which are precisely the edges of the
 1126 interfacial density layer.

1127 Due to the nature of shadowgraph images, and to its sensitivity to air bubbles or
 1128 scratches on the walls of the reservoirs, the identification of minima and maxima of
 1129 $I(z)$ could only be semi-automated according to the following methodology, illustrated
 1130 in figure B.1:

- 1131 (i) A random sample of typically three to five snapshots per movie were selected and
 1132 averaged (although in rare cases only one still image was available);
- 1133 (ii) A randomly-generated location in the streamwise direction was selected (dotted
 1134 blue lines) and the greyscale intensity profile $I(z)$ at this particular x location was
 1135 superimposed onto the image (solid red curves);
- 1136 (iii) The profile $I(z)$ was carefully interpreted, and the local extrema representing the
 1137 top and bottom duct boundaries (yellow crosses) and edges of the interface to
 1138 measure (circles) were carefully selected by a click.
- 1139 (iv) The ratio of pixel distances between the selected edges of the density interface and
 1140 the top and bottom walls was computed to yield δ .

1141 All images were processed by the first author to ensure consistency, and yielded a total
1142 of 351 values of δ for all four duct geometries (table 1).

1143 This methodology has at least two potential sources of error which we estimated to be
1144 relatively modest by performing an ad hoc set of additional measurements as we explain
1145 next.

1146 First, the determination of δ from averages of shadowgraph images may give artificially
1147 large results in flow with significant streamwise variations in the vertical position of the
1148 interfacial layer. To quantify this effect, we compared measurements of δ made using a
1149 single snapshot to those made using an average of three snapshots in five H flows and
1150 five T flows (including those in figure B.1(a),(c)), and performing each measurement
1151 at 10 random x locations (rather than one) to increase statistical robustness (total:
1152 $(5 + 5) \times 2 \times 10 = 200$ measurements). We found that H flows were most prone to this
1153 effect (as expected from waves distorting the interface), with δ being estimated in three-
1154 snapshot averages an average of 14 % above its single-snapshot value, compared to a
1155 more modest average of 7.5 % in T flows.

1156 Second, the determination of δ at a single x location may not give representative results
1157 in flows with significant streamwise variations in the thickness of their interfacial layer.
1158 To quantify this effect, we investigated the streamwise variability of δ using the same set
1159 of 200 additional measurements by focusing on the standard deviation (spread) around
1160 the mean of each set of 10 different x locations. We found that H flows had an average
1161 streamwise spread of 12 % of their mean, compared to a more modest 8.5 % in T flows.

1162 Note that measurements of δ in temperature-stratified experiments (mSIDT data
1163 set) could not be performed since the refractive index of water is a weaker function
1164 of temperature than salinity at comparable density differences, resulting in insufficient
1165 contrast and thus noisier $I(z)$ (sufficient to determine the flow regime but not δ).

1166 All interfacial thickness data (including a large number of still images, the code
1167 to determine δ , and the quantification of errors) are available on the repository
1168 doi.org/10.17863/CAM.48821.

1169 Appendix C. Frictional two-layer hydraulic model

1170 In this section we give details of the two-layer frictional hydraulic model introduced in
1171 § 5.2 and sketched in figure 9. This model is based on Gu (2001); Gu & Lawrence (2005)
1172 but includes non-zero tilt angles and a wider range of frictional stresses suited to the
1173 SID. We cover the model formulation in § C.1, the parameterisation of frictional effects
1174 in § C.2, and the solution to the full problem in § C.3.

1175 C.1. Model formulation

1176 The frictional hydraulic model appears at first inconsistent because it is based on
1177 velocities that are uniform in the cross-sectional plane ($\partial_{y,z}u_{1,2} = 0$), while implicitly
1178 acknowledging and parameterising the effects of viscous stresses resulting from $\partial_{y,z}u_{1,2} \neq$
1179 0. This model is however consistent provided that the departure from hydrostaticity is
1180 small (vertical and spanwise accelerations are negligible) and that viscous stresses are
1181 localised in relatively narrow boundary layers at the walls and interface ($Re \gg 50A$),
1182 rather than rather than through the whole volume ($Re < 50A$).

1183 Following standard hydraulic practice, the effective ‘hydraulic’ velocities $u_{1,2}(x)$ that
1184 will be used to compute the total Bernoulli head (kinetic energy) of each layer need to
1185 be defined in a way that accounts for the non-uniformity of the underlying ‘real’ velocity

1186 profile in the SID $u(x, y, z)$

$$u_{1,2}(x) \equiv \sqrt{\lambda_{1,2}(x) \langle u(x, y, z) \rangle_{y,z_{1,2}}}, \quad (\text{C1})$$

1187 where $\langle \cdot \rangle_{z_{1,2}}$ denotes averaging over the lower/upper layer ($z \in [-1, \eta]$ and $z \in [\eta, 1]$
1188 respectively, see figure 9(a)), and the velocity distribution coefficient $\lambda_{1,2}$ (also called
1189 kinetic energy correction coefficient or Coriolis coefficient) is defined as

$$\lambda_{1,2}(x) \equiv \frac{\langle u^3(x, y, z) \rangle_{y,z_{1,2}}}{\langle u(x, y, z) \rangle_{y,z_{1,2}}^3} > 1, \quad (\text{C2})$$

1190 respectively in the lower and upper layer (see e.g. Chow 1959, § 2.7-2.8 and Chanson
1191 2004, § 3.2.2). The greater the non-uniformity of the velocity profile u , the larger λ is.
1192 For the SID flows considered in this paper, volumetric velocity measurements showed
1193 that λ varies over a relatively small range $1 < \lambda \lesssim 2$ (see L18, § 5.5.2). To
1194 simplify the following discussion, and since the effects of λ are not central here (they
1195 quantitative rather than qualitative), we make the approximation that $\lambda_{1,2}(x) \approx 1$,
1196 effectively assuming that $u_{1,2}(x) = \langle u(x, y, z) \rangle_{y,z_{1,2}}$ in the following.

1197 First, the conservation of Bernoulli potential in two-layer hydraulic flows is commonly
1198 expressed using the so-called ‘internal energy’ of the system

$$E(x) \equiv \eta(x) + u_2^2(x) - u_1^2(x). \quad (\text{C3})$$

1199 Second, the conservation of volume and zero-net flux conditions are expressed all along
1200 the duct as

$$u_1(x)(1 + \eta(x)) = -u_2(x)(1 - \eta(x)) = Q. \quad (\text{C4})$$

1201 The third important ingredient of two-layer hydraulics is the condition of hydraulic
1202 control, which requires that the composite Froude number G is unity at sharp changes
1203 in geometry, i.e. at the duct ends (Armi 1986; Lawrence 1990):

$$G^2(x) \equiv 2 \left(\frac{u_1^2}{1 + \eta} + \frac{u_2^2}{1 - \eta} \right) = 4Q^2 \frac{1 + 3\eta^2}{(1 - \eta^2)^3} = 1 \quad \text{at } x = \pm A, \quad (\text{C5})$$

1204 where the second equality uses (C4) and the third equality is the control condition.

1205 In horizontal, frictionless ducts, $E(x) = 0$, hence $\eta = 0$ and $u_1 = -u_2 = Q = 1/2$ all
1206 along the duct.

1207 When the combined effects of a small positive tilt angle $\theta > 0$ and frictional stresses
1208 are added, the slope of the internal energy becomes

$$E'(x) = \eta'(x)(1 - G^2(x)) = \theta - S(x) \quad (\text{C6})$$

1209 (this is the two-layer equivalent of single-layer ideas found in (Henderson 1966, § 4.4-
1210 4.5)). By analogy with the topographic slope θ , the ‘frictional’ slope $S(x)$ is computed
1211 by a balance of all the stresses acting on an infinitesimal slice of thickness dx (figure
1212 9(b)):

$$S(x) = \frac{\sum_{\text{layer 1}}^{\text{stresses } j} \tau_1^j A_1^j}{V_1} + \frac{\sum_{\text{layer 2}}^{\text{stresses } j} \tau_2^j A_2^j}{V_2}. \quad (\text{C7})$$

1213 The subscript $i = 1, 2$ represents respectively the bottom and top layers, the superscript
1214 $j = Z, Y, I$ represents the origins of the stresses in the model: top and bottom wall stresses
1215 (Z , shown in blue in the figure), side wall stresses (Y , in green) and interfacial stresses
1216 (I , in red), A_i^j represents the surface area over which the respective stresses act, and
1217 V_i the volume of each layer. Note that the interfacial stresses have equal magnitudes on

1218 either sides of the interface $|\tau_1^I| = |\tau_2^I| \equiv \tau^I$. Following figure 9(b) and after elementary
1219 algebra, the balance in (C7) can be rewritten as:

$$S(x) = \frac{1}{1+\eta}\tau_1^Z + 2B^{-1}\tau_1^Y + \frac{1}{1+\eta}\tau^I + \frac{1}{1-\eta}\tau_2^Z + 2B^{-1}\tau_2^Y + \frac{1}{1-\eta}\tau^I. \quad (\text{C8})$$

1220 where all the stresses in this equation and henceforth are norms and have positive values.
1221 For further details about the development of this model from first principles, see L18,
1222 § 5.2.

1223 C.2. Parameterisation of shear stresses

1224 We now tackle the relation between the stresses τ_i^j and the underlying ‘real’ flow
1225 profiles $u(x, y, z)$. We start by considering the bottom wall stress of the lower layer τ_1^Z
1226 in order to introduce the key concepts and definitions, before extending them to the
1227 other stresses. Using non-dimensional variables for τ_1^Z and $u(x, y, z)$, we first write the
1228 *dimensional* equation for this stress as a simple function of the local shear

$$\left(\frac{\Delta U}{2}\right)^2 \tau_1^Z(x) = \nu \frac{\Delta U/2}{H/2} \left\langle \left| \frac{\partial u(x, y, z)}{\partial z} \right|_{z=-1} \right\rangle_y \quad (\text{C9})$$

1229 where the $\Delta U/2$ and $H/2$ factors come from non-dimensionalising τ_1^Z , u , z , and simplify
1230 to

$$\tau_1^Z(x) = \frac{1}{Re} \left\langle \left| \frac{\partial u(x, y, z)}{\partial z} \right|_{z=-1} \right\rangle_y. \quad (\text{C10})$$

1231 In order to correctly parameterise $\tau_1^Z(x)$ and all other relevant stresses using well-defined,
1232 constant friction coefficients, we follow the following five steps.

1233 (i) First, we define the cross-sectional ‘shape’ ($y - z$ dependence) of the local velocity
1234 profile in the lower layer as

$$\hat{u}_1(x, y, z) = \frac{u(x, y, z)}{u_1(x)}, \quad (\text{C11})$$

1235 such that $\langle \hat{u}_1(x, y, z) \rangle_{y, z_1} = 1$. This decomposition allows us to rewrite (C10) as

$$\tau_1^Z(x) = \frac{1}{Re} u_1(x) \left\langle \left| \frac{\partial \hat{u}_1(x, y, z)}{\partial z} \right|_{z=-1} \right\rangle_y, \quad (\text{C12})$$

1236 which is an exact expression for the local shear stress that does not require any assump-
1237 tions about the value of the velocity gradient or flow profile.

1238 (ii) Second, we define a ‘layer-rescaled’ coordinate \hat{z}_1 as

$$\hat{z}_1 := \frac{z}{1+\eta} = z \frac{Q}{u_1(x)}, \quad (\text{C13})$$

1239 in which layer 1 always has thickness one ($\hat{z}_1 \in [-1, 0]$), giving us

$$\tau_1^Z(x) = \frac{1}{Re} \frac{u_1^2(x)}{Q} \left\langle \left| \frac{\partial \hat{u}_1(x, y, \hat{z}_1)}{\partial \hat{z}} \right|_{\hat{z}_1=-1} \right\rangle_y. \quad (\text{C14})$$

1240 (iii) Third, we define a constant, bottom friction parameter f_{Z_1} to parameterise the stress:

1241

$$\tau_1^Z(x) = \frac{f_{Z_1}}{Re} \frac{u_1^2(x)}{Q} \quad \text{with} \quad f_{Z_1} \equiv \left\langle \left| \frac{\partial \hat{u}_1(x, y, \hat{z}_1)}{\partial \hat{z}} \right|_{\hat{z}_1=-1} \right\rangle_{x, y}. \quad (\text{C15})$$

1242 We note that despite the rescaling of $u(x, y, z)$ by $u_1(x)$ and the stretching of z to \hat{z}_1
1243 such that the interface is located at $\hat{z}_1(x) = 0$, \hat{u}_1 still has a weak residual x dependence.

1244 Since for simplicity, we choose to model f_{Z_1} as independent of x , the velocity gradient
 1245 $\partial\hat{u}_1(x, y, z)/\partial\hat{z}|_{\hat{z}_1=-1}$ must now technically be averaged not only over y but over x and
 1246 y , as shown in (C 15). We also note that the $u_1^2(x)/Q$ factor in (C 15) results from the
 1247 product of $u_1(x)$ (by definition of \hat{u}_1) by $u_1(x)/Q$ (by definition of \hat{z}_1). Physically, this
 1248 quadratic dependence corresponds to the vertical shear being enhanced not only by the
 1249 magnitude of u_1 , but also by the enhanced vertical gradient due to the thinner layers
 1250 where u_1 is larger. This $u_1^2(x)/Q$ scaling will be found in the interfacial stress τ^I too.
 1251 However, the equivalent formulation to (C 14) for the side wall stress in layer 1, τ_1^Y , is

$$\tau_1^Y(x) = \frac{1}{Re} u_1(x) \left\langle \left| \frac{\partial\hat{u}_1(x, y, z)}{\partial y} \right|_{y=\pm 1} \right\rangle_{z_1}, \quad (\text{C } 16)$$

1252 where we assume identical shear at $y = \pm 1$. We emphasise that since the y derivative
 1253 does not experience any rescaling due to the layer thickness, it follows a $u_1(x)$ scaling
 1254 (as opposed to $u_1^2(x)/Q$ for z derivatives).
 1255 (iv) Fourth, we generalise the above definitions of \hat{u}_1 and \hat{z}_1 to both layers by defining a
 1256 global \hat{u} as

$$\hat{u}(x, y, z) := \begin{cases} \frac{u(x, y, z)}{u_1(x)} & \text{for } z \in [-1, \eta], \\ \frac{u(x, y, z)}{u_2(x)} & \text{for } z \in [\eta, 1], \end{cases} \quad (\text{C } 17)$$

1257 and a global \hat{z} as

$$\hat{z} := \begin{cases} \frac{z}{1+\eta} = z \frac{Q}{u_1(x)} & \text{for } z \in [-1, \eta], \\ \frac{z}{1-\eta} = z \frac{Q}{u_2(x)} & \text{for } z \in [\eta, 1]. \end{cases} \quad (\text{C } 18)$$

1258 (v) Fifth, we consider the role of turbulence at the interface, caused by Reynolds stresses
 1259 which we parameterise, by analogy with (C 10), as follows

$$\langle -\hat{u}'w' \rangle_{x, y, z_I, t} = \frac{1}{Re} K_I \left\langle \frac{\partial(\hat{u})_{xyt}}{\partial\hat{z}} \right\rangle_{z_I}, \quad (\text{C } 19)$$

1260 where $\mathbf{u}' \equiv \mathbf{u} - \langle \mathbf{u} \rangle_t$ is the perturbation around the temporal mean and K_I the
 1261 turbulent momentum diffusivity non-dimensionalised by the molecular value ν . Under
 1262 these conditions, the total (molecular + turbulent) interfacial stress τ^I can be expressed
 1263 precisely as:

$$\tau^I(x) = \frac{1 + K_I}{Re} \frac{(u_1(x) - u_2(x))^2}{Q} \left\langle \left| \frac{\partial\hat{u}(x, y, \hat{z})}{\partial\hat{z}} \right| \right\rangle_{y, \hat{z}_I}, \quad (\text{C } 20)$$

1264 where \hat{z}_I denotes averaging over the interfacial mixed layer.

Based on the five above steps, we propose the following parameterisation of frictional effects in the hydraulic model

$$\tau_{1,2}^Z(x) = \frac{f_Z}{Re} \frac{u_{1,2}^2(x)}{Q}, \quad (\text{C } 21a)$$

$$\tau_{1,2}^Y(x) = \frac{f_Y}{Re} |u_{1,2}(x)|, \quad (\text{C } 21b)$$

$$\tau_1^I(x) = \tau_2^I(x) = \frac{f_I}{Re} \frac{(u_1(x) - u_2(x))^2}{Q}. \quad (\text{C } 21c)$$

where the vertical, spanwise and interfacial friction parameters are, respectively,

$$f_Z \equiv \left\langle \left| \frac{\partial \hat{u}(x, y, \hat{z})}{\partial \hat{z}} \right|_{\hat{z}=\pm 1} \right\rangle_{xy}, \quad (\text{C } 22a)$$

$$f_Y \equiv \left\langle \left| \frac{\partial \hat{u}(x, y, \hat{z})}{\partial y} \right|_{y=\pm 1} \right\rangle_{xz}, \quad (\text{C } 22b)$$

$$f_I \equiv (1 + K_I) \left\langle \left| \frac{\partial \hat{u}(x, y, \hat{z})}{\partial \hat{z}} \right| \right\rangle_{x,y,z_I}. \quad (\text{C } 22c)$$

1265 The y and \hat{z} derivatives at $y, \hat{z} = \pm 1$ should be very similar, and the average of the
1266 two is implied. The three parameters can be computed from three-dimensional, three-
1267 component velocity measurements, as was done in L18, § 5.5.

1268 C.3. Key equations and solution method

1269 We can now rewrite the frictional slope $S(x)$ in (C 8) using (C 22) and (C 4) as

$$Re S(x) = \frac{2Qf_Z}{(1 - \eta^2)^3} \left\{ (1 + 3\eta^2) + 2\frac{f_Y}{f_Z} B^{-1} (1 - \eta^2)^2 + 8\frac{f_I}{f_Z} \right\}. \quad (\text{C } 23)$$

1270 By combining this expression for $S(x)$ with the expression for the composite Froude
1271 number $G^2(x)$ in (C 5) we finally obtain an expression for the differential equation
1272 governing the evolution of the interfacial slope $\eta'(x)$ in (C 6)

$$\eta'(x) = \frac{\theta Re(1 - \eta(x)^2)^3 - 2Qf_Z\{1 + 3\eta^2(x) + 2r_Y(1 - \eta^2(x))^2 + 8r_I\}}{Re\{(1 - \eta(x))^2\}^3 - 4Q^2(1 + 3\eta^2(x))}, \quad (\text{C } 24)$$

1273 where the spanwise friction ratio r_Y and interfacial friction ratio r_I are defined under
1274 (5.4). This equation was simplified to (5.3) for the discussion in § 5.2.

1275 The idea behind the solution to this kind of problem can essentially be found in Gu
1276 & Lawrence (2005). However, contrary to their model (which had no tilt angle and no
1277 top and side wall friction $\theta = f_{Z1} = f_Y = 0$), our model does not allow us to find an
1278 analytical solution to (C 24). We must therefore resort to an iterative numerical approach
1279 which we briefly outline below.

1280 By symmetry of the problem (guaranteed under the Boussinesq approximation), η is
1281 an odd function of x . We impose the boundary condition $\eta(0) = 0$ and need only solve
1282 (C 24) in half of the domain (say $x \in [0, A]$).

1283 However, since the volume flux Q in (C 24) is a priori unknown, we must solve a
1284 coupled problem imposing the additional condition of hydraulic control at each duct end
1285 (denoted by the superscript *)

$$G^{*2} \equiv G^2(-\eta^*) = 4Q^2 \frac{1 + 3\eta^{*2}}{(1 - \eta^{*2})^3} = 1 \quad \implies \quad Q = \frac{1}{2} \sqrt{\frac{(1 - \eta^{*2})^3}{1 + 3\eta^{*2}}}, \quad (\text{C } 25)$$

1286 where η^* is the result of the forward integration of (C 24)

$$\eta^* \equiv \eta(-A) = -\eta(A) = - \int_0^A \eta'(Q, \theta, f_Z, r_Y, r_I) dx > 0. \quad (\text{C } 26)$$

1287 The coupled problem for $\eta(x)$ and Q for any given set of forcing and friction parameters
1288 $(\theta, Re, f_Z, r_Y, r_I)$ can then be solved by the following iterative algorithm (illustrated in
1289 L18, figure 5.4).

- 1290 (i) Guess Q ;
- 1291 (ii) Integrate numerically (C 24) from $x = 0$ to A to get η^* as in (C 26);

- 1292 (iii) Get the Q corresponding to this η^* by the criticality condition (C25);
 1293 (iv) Compare this Q with the initial guess and update the guess;
 1294 (v) Repeat until convergence of Q .
 1295 This model and its solution were validated using parameters ($\theta, Re, f_Z, r_Y, r_I$) from an
 1296 experiment in the L regime, and quantitative agreement with $\eta(x)$ and Q measurements
 1297 was found L18, § 5.5.3.

REFERENCES

- 1298 ANATI, D. A., ASSAF, G. & THOMPSON, R. 1977 Laboratory models of sea straits. *Journal of*
 1299 *Fluid Mechanics* **81**, 341–351.
 1300 ARMI, L. 1986 The hydraulics of two flowing layers with different densities. *Journal of Fluid*
 1301 *Mechanics* **163**, 27–58.
 1302 ASSAF, G. & HECHT, A. 1974 Sea straits: a dynamical model. *Deep-sea Research* **21**, 947–958.
 1303 DE BRUYN KOPS, S. M. 2015 Classical scaling and intermittency in strongly stratified Boussinesq
 1304 turbulence. *Journal of Fluid Mechanics* **775**, 436–463.
 1305 CAULFIELD, C. P. 1994 Multiple linear instability of layered stratified shear flow. *Journal of*
 1306 *Fluid Mechanics* **258**, 255–285.
 1307 CHANSON, H. 2004 *The hydraulics of open channel flows: an introduction*, 2nd edn. Elsevier.
 1308 CHOW, V. T. 1959 *Open-channel hydraulics*. McGraw-Hill, New York.
 1309 CORMACK, D. E., LEAL, L. G. & IMBERGER, J. 1974a Natural convection in a shallow cavity
 1310 with differentially heated end walls. Part 1. Asymptotic theory. *Journal of fluid Mechanics*
 1311 **65**, 209–229.
 1312 CORMACK, D. E., LEAL, L. G. & SEINFELD, J. H. 1974b Natural convection in a shallow
 1313 cavity with differentially heated end walls. Part 2. Numerical solutions. *Journal of Fluid*
 1314 *Mechanics* **65**, 231–246.
 1315 DALZIEL, S. B. 1991 Two-layer hydraulics: a functional approach. *Journal of Fluid Mechanics*
 1316 **223**, 135–163.
 1317 DEACON, M. 1971 *Scientists and the Sea 1650-1900, A Study of Marine Science*. Academic
 1318 Press, London.
 1319 ENGQVIST, A. 1996 Self-similar multi-layer exchange flow through a contraction. *Journal of*
 1320 *Fluid Mechanics* **328**, 49–66.
 1321 ESTRADA, M. 1996 Primary production in the northwestern Mediterranean. *Scientia marina*
 1322 **60**, 55–64.
 1323 GU, L. 2001 Frictional exchange flow through a wide channel with application to the Burlington
 1324 ship canal. PhD thesis, The University of British Columbia.
 1325 GU, L. & LAWRENCE, GREGORY A. 2005 Analytical solution for maximal frictional two-layer
 1326 exchange flow. *Journal of Fluid Mechanics* **543**, 1–17.
 1327 HELFRICH, K. R. 1995 Time-dependent two-layer hydraulic exchange flows. *Journal of Physical*
 1328 *Oceanography* **25** (3), 359–373.
 1329 HENDERSON, F. M. 1966 *Open channel flow*. MacMillan, New York.
 1330 HOGG, A. M., IVEY, G. N. & WINTERS, K. B. 2001 Hydraulics and mixing in controlled
 1331 exchange flows. *Journal of Geophysical Research: Oceans* **106** (C1), 959–972.
 1332 HOGG, A. MCC. & KILLWORTH, P. D. 2004 Continuously stratified exchange flow through a
 1333 contraction in a channel. *Journal of Fluid Mechanics* **499**, 257–276.
 1334 HOLMBOE, J. 1962 On the behavior of symmetric waves in stratified shear layers. *Geophys. Publ.*
 1335 **24**, 67–113.
 1336 HUGHES, G. O. & LINDEN, P. F. 2016 Mixing efficiency in run-down gravity currents. *Journal*
 1337 *of Fluid Mechanics* **809**, 691–704.
 1338 IMBERGER, J. 1974 Natural convection in a shallow cavity with differentially heated end walls.
 1339 Part 3. Experimental results. *Journal of Fluid Mechanics* **65**, 247–260.
 1340 KIEL, D. E. 1991 Buoyancy driven counterflow and interfacial mixing. PhD thesis, University
 1341 of Cambridge.
 1342 LANE-SERFF, G. F., SMEED, D. A. & POSTLETHWAITE, C. R. 2000 Multi-layer hydraulic
 1343 exchange flows. *Journal of Fluid Mechanics* **416**, 269–296.

- 1344 LAWRENCE, G. A. 1990 On the hydraulics of Boussinesq and non-Boussinesq two-layer flows.
1345 *Journal of Fluid Mechanics* **215**, 457–480.
- 1346 LEACH, S. J. & THOMPSON, H. 1975 An experimental investigation of some aspects of flow
1347 into a gas cooled nuclear reactors following an accidental depressurization. *Journal of the*
1348 *British Nuclear Energy Society* **14** (3), 243–250.
- 1349 LEFAUVE, A. 2018 Waves and turbulence in sustained stratified shear flows. PhD thesis,
1350 University of Cambridge. doi:10.17863/CAM.24648.
- 1351 LEFAUVE, A., PARTRIDGE, J. L. & LINDEN, P. F. 2019 Regime transitions and energetics of
1352 sustained stratified shear flows. *Journal of Fluid Mechanics* **875**, 657–698.
- 1353 LEFAUVE, A., PARTRIDGE, J. L., ZHOU, Q., CAULFIELD, C. P., DALZIEL, S. B. & LINDEN, P. F.
1354 2018 The structure and origin of confined Holmboe waves. *Journal of Fluid Mechanics*
1355 **848**, 508–544.
- 1356 LINDEN, P. F. 1999 The fluid mechanics of natural ventilation. *Annual Review of Fluid*
1357 *Mechanics* **31**, 201–238.
- 1358 LUCAS, D., CAULFIELD, C. P. & KERSWELL, R. R. 2017 Layer formation in horizontally forced
1359 stratified turbulence: connecting exact coherent structures to linear instabilities. *Journal*
1360 *of Fluid Mechanics* **832**, 409–437.
- 1361 MACAGNO, E. O. & ROUSE, H. 1961 Interfacial mixing in stratified flow. *Journal of the*
1362 *Engineering Mechanics Division. Proceeding of the American Society of Civil Engineers*
1363 **87** (EM5), 55–81.
- 1364 MERCER, A. & THOMPSON, H. 1975 An experimental investigation of some further
1365 aspects of buoyancy-driven exchange flow between carbon dioxide and air following a
1366 depressurization accident in a Magnox reactor; Part 1: The exchange flow in inclined
1367 ducts. *Journal of the British Nuclear Energy Society* **14** (4), 327–334.
- 1368 MEYER, C. R. & LINDEN, P. F. 2014 Stratified shear flow: experiments in an inclined duct.
1369 *Journal of Fluid Mechanics* **753**, 242–253.
- 1370 PARTRIDGE, J. L., LEFAUVE, A. & DALZIEL, S. B. 2019 A versatile scanning method
1371 for volumetric measurements of velocity and density fields. *Measurement Science and*
1372 *Technology* **30**, 055203.
- 1373 PELTIER, W. R. & CAULFIELD, C. P. 2003 Mixing efficiency in stratified shear flows. *Annual*
1374 *Review of Fluid Mechanics* **35** (1), 135–167.
- 1375 PORTWOOD, G. D., DE BRUYN KOPS, S. M., TAYLOR, J. R., SALEHIPOUR, H. & CAULFIELD,
1376 C. P. 2016 Robust identification of dynamically distinct regions in stratified turbulence.
1377 *Journal of Fluid Mechanics* **807**, R2.
- 1378 PRASTOWO, T., GRIFFITHS, R. W., HUGHES, G. O. & HOGG, A. M. 2008 Mixing efficiency in
1379 controlled exchange flows. *Journal of Fluid Mechanics* **600**.
- 1380 REYNOLDS, O. 1883 An experimental investigation of the circumstances which determine
1381 whether the motion of water shall be direct or sinuous, and of the law of resistance in
1382 parallel channels. *Philosophical Transactions of the Royal Society of London* **174**, 935–982.
- 1383 SALEHIPOUR, H., CAULFIELD, C. P. & PELTIER, W. R. 2016 Turbulent mixing due to the
1384 Holmboe wave instability at high Reynolds number. *Journal of Fluid Mechanics* **803**,
1385 591–621.
- 1386 SALEHIPOUR, H. & PELTIER, W. R. 2015 Diapycnal diffusivity, turbulent Prandtl number and
1387 mixing efficiency in Boussinesq stratified turbulence. *Journal of Fluid Mechanics* **775**,
1388 464–500.
- 1389 SALEHIPOUR, H., PELTIER, W. R. & C. P. CAULFIELD, C. P. 2018 Self-organized criticality of
1390 turbulence in strongly stratified mixing layers. *Journal of Fluid Mechanics* **856**, 228–256.
- 1391 SCHIJF, J. B. & SCHÖNFLED, J. C. 1953 Theoretical considerations on the motion of salt and
1392 fresh water. In *Proceedings Minnesota International Hydraulic Convention*. IAHR.
- 1393 SHERMAN, F. S., IMBERGER, J. & CORCOS, G. M. 1978 Turbulence and mixing in stably
1394 stratified waters. *Annual review of fluid mechanics* **10** (1), 267–288.
- 1395 SMYTH, W. D. & MOUM, J. N. 2013 Marginal instability and deep cycle turbulence in the
1396 eastern equatorial Pacific Ocean. *Geophysical Research Letters* **40** (23), 6181–6185.
- 1397 STOMMEL, H. & FARMER, H. G. 1953 Control of salinity in an estuary by a transition. *Journal*
1398 *of Marine Research* **12** (1), 13–20.
- 1399 TAYLOR, G. I. 1931 Effect of Variation in Density on the Stability of Superposed Streams

- 1400 of Fluid. *Proceedings of the Royal Society A: Mathematical, Physical and Engineering*
1401 *Sciences* **132** (820), 499.
- 1402 TAYLOR, J. R., DEUSEBIO, E., CAULFIELD, C. P. & KERSWELL, R. R. 2016 A new method
1403 for isolating turbulent states in transitional stratified plane Couette flow. *Journal of Fluid*
1404 *Mechanics* **808**, R1.
- 1405 THORPE, S. A. & LIU, ZHIYU 2009 Marginal Instability? *Journal of Physical Oceanography*
1406 **39** (9), 2373–2381.
- 1407 WILKINSON, D. L. 1986 Buoyancy driven exchange flow in a horizontal pipe. *Journal of*
1408 *Engineering Mechanics* **112** (5), 485–497.
- 1409 WINTERS, K. B., LOMBARD, P. N., RILEY, J. J. & D'ASARO, E. A. 1995 Available potential
1410 energy and mixing in density-stratified fluids. *Journal of Fluid Mechanics* **289**, 115–128.
- 1411 WINTERS, K. B. & SEIM, H. E. 2000 The role of dissipation and mixing in exchange flow
1412 through a contracting channel. *Journal of Fluid Mechanics* **407**, 265–290.
- 1413 WOOD, I. R. 1968 Selective withdrawal from a stably stratified fluid. *Journal of Fluid Mechanics*
1414 **32** (02), 209–223.
- 1415 WOOD, I. R. 1970 A lock exchange flow. *Journal of Fluid Mechanics* **42** (04), 671–687.
- 1416 ZHOU, Q., TAYLOR, J. R., CAULFIELD, C. P. & LINDEN, P. F. 2017 Diapycnal mixing in
1417 layered stratified plane Couette flow quantified in a tracer-based coordinate. *Journal of*
1418 *Fluid Mechanics* **823**, 198–229.
- 1419 ZHU, D. Z. & LAWRENCE, GREGORY A. 2000 Hydraulics of exchange flows. *Journal of Hydraulic*
1420 *Engineering* **126** (12), 921–928.